Solar Energy: Potential and Toxicology

1

Bhumika Ancha, Sajid Bashir, Nancy KingSanders, and Jingbo Louise Liu

This chapter is dedicated to Professor Peter J. Derrick who passed away in March 2017 during the writing of this chapter.

Contents

1.1 Introduction 3
1.2 Solar Energy 5
1.3 Solar Thermal Electricity (STE) and Solar Photovoltaics (PV) 9
1.4 Solar Cell Primer 13
1.5 Toxicological Evaluation 18
1.6 Photocatalytic Reactivity 21

Author Contribution

BA completed all the experimental research, and the experimental, result, and conclusion sections with the first draft of the introduction were written by LL. The data in the figures and charts in the introduction were supplied by SB and LL. The final draft was reviewed and edited by NKS and LL.

B. Ancha · S. Bashir
Department of Chemistry, Texas A&M University-Kingsville, Kingsville, TX, USA
e-mail: bhumika.ancha@students.tamuk.edu; kfsb005@tamuk.edu

N. KingSanders
Austin Peay State University, Clarksville, TN, USA
e-mail: kingsandersn@apsu.edu

J. L. Liu (✉)
Department of Chemistry, Texas A&M University-Kingsville, Kingsville, TX, USA

Department of Chemistry, Texas A&M University (TAMU), College Station, TX, USA
e-mail: kfjll00@tamuk.edu; jingbo.liu@tamu.edu

© Springer-Verlag GmbH Germany, part of Springer Nature 2019

T. A. Atesin et al. (eds.), *Nanostructured Materials for Next-Generation Energy Storage and Conversion*, https://doi.org/10.1007/978-3-662-59594-7_1

1.7 Bactericidal Properties 22
1.7.1 Experimental Procedure 22
1.7.2 Synthesis Overview 23
1.7.3 Colloidal Synthesis 23
1.7.4 Solid State Chemistry to Produce CTO-NPs 24
1.7.5 Characterization of Titania 24
1.7.6 X-Ray Powder Diffraction 24
1.7.7 Transmission and Scanning Electron Microscopy 25
1.7.8 Spectroscopic Analyses 25
1.7.9 Bactericidal Performance of CTO-NPs 26
1.8 Results 27
1.8.1 Synthesis of CTO-NPs 27
1.8.2 Characterization of Titania 27
1.8.3 X-Ray Powder Diffraction 27
1.8.4 Transmission and Scanning Electron Microscopy 28
1.8.5 X-Ray Energy Dispersive Spectroscopy 28
1.8.6 Applications of Nanomaterials 31
1.8.7 Photocatalytical Reactivities of CTO-NPs 31
1.8.8 Bactericidal Performance of CTO-NPs 33
1.9 Discussion 34
1.9.1 Colloidal and Solid State Chemistry 34
1.9.2 Characterization of Titania 36
1.9.3 Application of Nanomaterials 38
1.10 Conclusion 38
References 39

Abstract

Global energy demands towards 100 PW necessitated a rethink of approaches to generate the required demand through accelerated use of sustainable resources for both heating and generation of electricity. This is to degrade the global warming potential, lower greenhouses gases, and ultimately ensure against depletion of natural resources which may be required for habituation, agro-use or extraction for construction, catalysis, and fabrication of new materials instead of energy. Of the newer types of sustainable resources, solar energy has drawn considerable interest, due to the ability of the sun (a nuclear fusion reactor) to potentially meet all the demands with regard to heating and electrical generation. Current global production of electricity via solar only top 100 GW (less than 10% of the required load) but show promise. Current solar technologies are dominated by crystal silicon solar cells, although newer approaches using thin-films, CdTe, organic photopolymers, and composite devices have come online to meet the anticipated share for energy and heating, in diverse applications (satellite communication, heating, desalination, pumping of water, and electricity generation). While solar cells directly do not generate carbon dioxide and contribute towards global warming, the manufacturing of these devices does expend considerable energy and generates carbon dioxide, although levelized costs (dollar-per-kilowatt hour) are comparable to a coal-derived generation of energy and the roll-out and market deployment of solar cells is expected to increase. Likewise the environmental and

health hazard of disposal of solar components at end-of-life is unknown due to their longevity (25–30 year life cycle), although preliminary studies have shown that semiconductor components such as titania (TiO_2) are toxic to human cells, microorganism, and freshwater algae, there is considerable variation in lethality of titania, due to exposure, concertation, and type of titania (anatase or rutile, nano or bulk) and microorganism (Gram-negative or Gram-positive).

To address the question of toxicity, we undertook synthesis, characterization, photocatalyticity, and cytotoxicity of Ce-doped TiO_2 (CTO-NPs). An environmental-friendly and cost-effective sol-gel approach was used to prepare different formulations of CTO-NPs. The starting materials of $Ce(NO_3)_3$ and $Ti(OBu)_4$ were used, and a water-isopropanol mixture was used as a solvent to ensure the solubility of the above starting materials. The fabrication variables of CTO-NPs were optimized according to the photocatalytic reactivity and antibacterial activities. The powders of CTO-NPs were prepared after calculation at 200–400 °C with an increment of 50 °C for 2 h. These so-prepared CTO-NPs were characterized using X-ray powder diffraction, scanning and transmission electron microscopy, and ultraviolet and Raman spectroscopy, to evaluate their crystalline structure, morphology, and vibrational modes. It was found that the TiO_2 tetragonal anatase structure (PDF 01-086-1157, 3.7852 × 9.5139 Å and 90 × 90°) was obtained. The cerium cation-substituted the lattice Ti, leading to one phase formation. These CTO-NPs were found to be effective at decomposing methylene blue under visible light. Both Gram-negative (*S. marcescens*, ATCC 49732) and Gram-positive (*M. luteus*, ATCC 13880) bacteria were also tested using CTO-NPs as disinfectants. The maximum bactericidal concentrations (MBCs) were found to be 0.6 ppm to inactivate both bacteria within 1 h.

1.1 Introduction

The total energy needs of the planet are approximately 14,200 million metric tons of oil equivalent (TOE) or 165 PW/h in 2017 (1 PW/h = 1×10^{15} W/h) [1]. Of this approximately 3.9% is from renewable resources (excluding hydro and nuclear), 4.6% from nuclear, 7.0% from hydro, 24.2% from gas, 27.9% from coal, and 32.4% from oil [2]. Relative to 1972 when almost 50% of the energy was from oil, all primary energy sources have declined except gas and renewables. Coal has fluctuated up and is expected to decline after 2020 to be surpassed by gas as the primary energy resource (after oil) as the next highest source [3]. Nuclear source spiked from approximately 1980s to 2010 and is now stable at 4%. It is the significant rise of renewables that is of interest, this rise becoming significant around 2020 and by 2040 comprising 14% of global energy.

Where does solar fit in? Solar and wind is the major primary energy sources for renewables accounting for 1.4% compared to 2.3% for wind or 0.07 million TOE for solar and 0.14 million TOE for wind, however. This current capacity is a fraction of the actual energy output of our sun, a yellow dwarf star that has a surface temperature

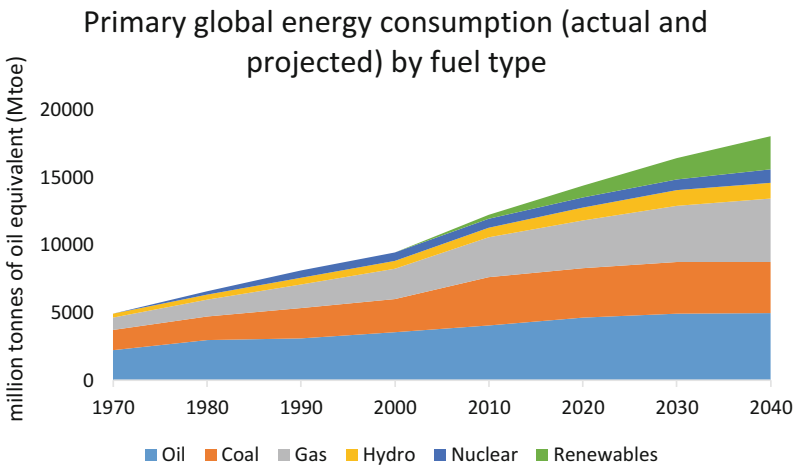

Fig. 1.1 Summary of global energy by fuel type by decade. (Sources: [5–7])

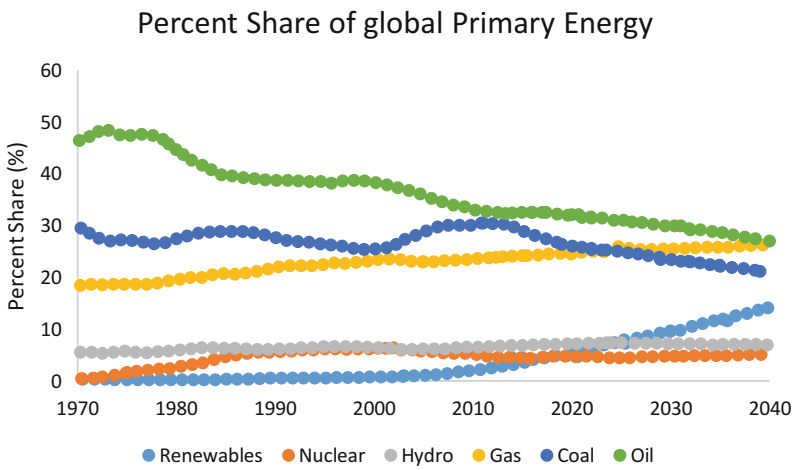

Fig. 1.2 Summary of percent share of global energy by fuel type by decade. (Sources: [5–8])

of approximately 5700 K and an energy of almost 3,300,000 YWh (1 YWh = 1 × 10^{24} Wh), which is less than the entire combined energy need of the plant [4] shown in Figs. 1.1 and 1.2.

The vast majority of energy is derived from fossil fuels (~92%), leaving nuclear and hydro with 8% in the 1980s to an anticipated 12% by 2020 with other renewables being less than 0.1% in the 1970s rising to 17% by 2020 (nuclear, hydro, solar, wind, and thermal storage). While not significant in statistical terms, it is a great increase relative to initial usage [9–11].

Primary energy can broadly be classified as non-renewables and includes fossil fuels, minerals and biomass, and renewables that include solar, wind, thermal, and hydro.

The former category is dependent upon mining, extraction, purification (or fractionation), and usage, whereas the renewables resources rely on weather and rainfall to generate energy [12]. Oil exploration peaked in 2006 and is expected to decline slowly until 2040 for conventional oil. Moving to natural gas liquids, utilization of horizontal drilling and hydraulic fracturing into liquids-rich sweet spots of shale and tight gas will extend the utility of fossil fuels, but this is a tradeoff between economics of extraction, cracking, transportation, compliance, and resale, and as reserves dwindle, the more technically challenging "expensive" pockets would need to be explored, driving up costs. The extraction process is also expensive in terms of brine used, and combustion of fuels to generate energy and carbon dioxide and water [13].

1.2 Solar Energy

Sunlight is a resource that could be further tapped and utilized. Plants and certain algae utilize sunlight to generate sugars during photosynthesis. Unfortunately, not all sunlight is used to the same degree [14]. The planet Earth is oval shaped with a natural curvature. Some of the irradiances are reflected (30%), another 29% is absorbed by the atmosphere or reflected by clouds or the atmosphere, in addition to being radiated into space from the atmosphere or the land. Some of the sunlight is used in conduction and rising air (6.8%), another 22.9% is used to heat water (latent heat of vaporization) leaving 51% to be absorbed by surface (plants, land or oceans); approximately 15 PW/h is available for heating and conversion into biomass, or electricity [15]. The global demand for energy was 138 TW/h meaning the solar could supply all planetary energy needs, even at 75% emission loss [16].

The fraction of light energy that falls on the surface is a factor of longitude and latitude as well as the time of year. This is because the plant is oval and the sun is spherical, with the planet orbiting the sun once every 365 days (~ 4380 h of illumination per year) with an axis of rotation of 23.45° to the orbital plane [17]. The light rays travel a greater distance when the sun is "lower" in the sky than its zenith. The light intensity falling on the surface can be approximated using a cosine function (irradiance is equal to irradiance on a surface perpendicular to the direction of the sun x the cosine of the irradiance angle) of 23.45° and is independent on atmospheric adsorption [4].

For example, sunlight impact at a 60° angle has to travel twice as far as overhead. This "air mass" (value of 2) relative to a value of 1 (overhead at zenith) would also lower the light energy due to absorption, refraction, and scattering by the atmosphere, which absorbs most if not all of the shorter wavelengths such as ultraviolet radiation. The sunlight of the most practical use is visible, near infrared. Taking water as an example to illustrate how the electromagnetic radiation affects chemical processes, the dissociation bind energy is approximately 290 kJ/mol [18] shown in Fig. 1.3a, b.

Light absorption would excite electrons into higher electronic states, and in Fig. 1.3c it can be seen that ultraviolet radiation would have sufficient energy, it can also be seen that the bulk of this energy is screened (e.g., by ozone) and never

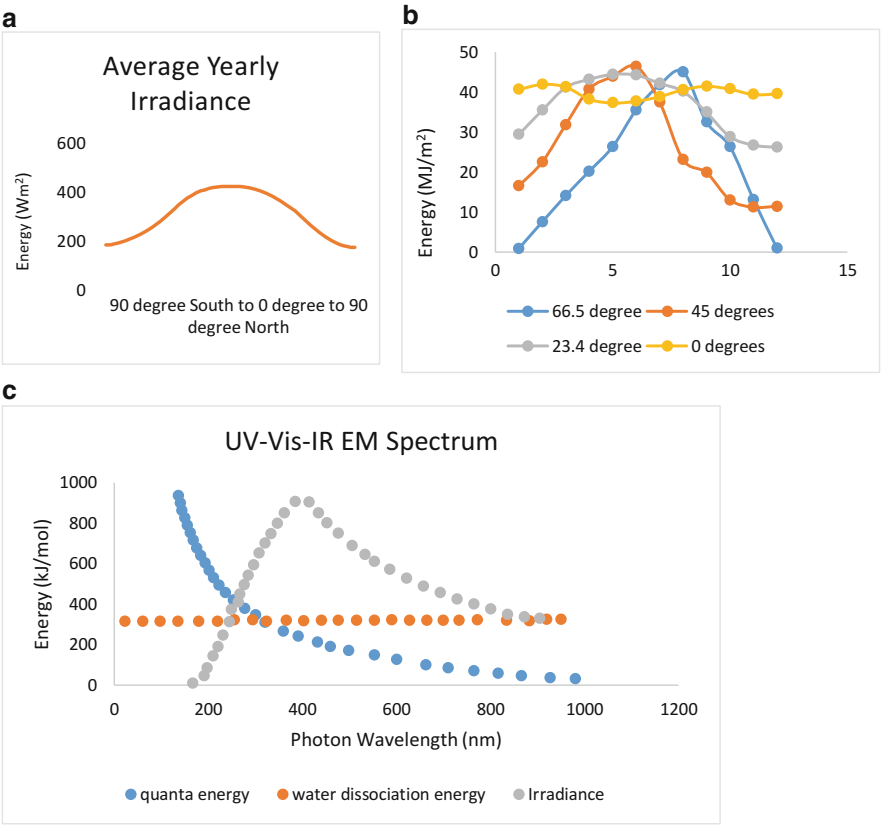

Fig. 1.3 Breakdown of electromagnetic radiation by (**a**) latitude, (**b**) tilt angle, (**c**) and function of quanta energy versus wavelength, irradiance, and energy required to dissociate water by one or multiple photon-absorption events. (Source: [18])

reaches the surface. Therefore, although UV radiation is capable of bond dissociation, statistically this is an unlikely event due to the lower intensity reaching oceans and lakes near the surface, whereas visible light photons do not have sufficient energy if a one-step process is considered. For visible light to be effective, a multi-step process is required, where multiple quanta of energy are required. This, in turn, will lower the efficiency of the reaction. Although the absorption of blue and red light by plants is a multi-step process and is inefficient relative to a single quantum process efficiencies, the sheer quantity of photons and plants enable this to be a productive process. The last point is an important consideration; water, for example, is transparent to visible light and would require a photocatalyst to absorb the incident light energy to transfer this energy to the molecule to facilitate bond cleavage. For an efficient process, this would also require the catalyst to have high absorptivity and broad spectral response. Since the plant is curved and spinning on its axis, the average irradiance is not constant but depends on the tilt angle. The regions which

receive the highest flux are Africa (7 °N and 21 °E), South America (23 °N/102 °W), and Australia (27 °S/133 °E). The optimal tilt angle for light collection can be defined either as global normal irradiance (GNI) or direct normal irradiance (DNI). The former relates to a measure of the maximum solar energy that can be used, while the latter relates to the irradiance received on a surface perpendicular to the sun's light (in the form of electromagnetic (EM) radiation) [19]. Tilt angles can become significant between 30 °S and 30 °N and may be up to 15° lower than latitude, affecting design and construction. The difference in collected energy between no tilt angle and where the sun's rays are tracked could be as much as threefold, and this difference is expected to be more pronounced in Europe, and less in Africa, Australia, and South Pacific. The average sunlight is dependent upon the broad longitude/latitude instead of a constant and also highly dependent upon the season. It varies from 1200 kWh/m^2/year in Europe to 1800 kWh/m^2/year in Central America, Australia, and Africa to 2300 kWh/m^2 during the summer months [20]. The irradiation of sunlight on the earth's surface is not uniform or constant over one rotation and thus needs to be averaged to decide if a specific location is suitable to harvest sunlight. This is accomplished by using global normal irradiance as a starting point in the calculation to determine the actual sunlight at a specific location over a specified period (day, week, month or year). The GNI value is approximated as 500 kWh/ m2 /year, from which the "average" is calculated around 1300 W/m2. This value is estimated using the expression (1.1):

$$I = F_c\left[1 + xcos\left(2\pi\frac{\text{day} - 3}{365}\right]\right. \tag{1.1}$$

where I is the solar irradiance, adjusted for eccentricity which in turn is related to Earth's position relative to the sun, as it orbits the sun (day 1–365). The solar flux constant (F_c) is 128 × 10^3 lux. The DNI correction for the atmosphere is DNI $= F_c e^{-\text{cm}}$, where c is the atmospheric extinction coefficient (e.g., 4.61 m^{-1}) and varies by depth, while m is the relative optical air mass (e.g., AM1.5 W/m^2; Fig. 1.4). A day is defined as the time interval between two successive transits by the sun over a specific location (for example, the meridian) corresponding to one diurnal cycle or full rotation of the Earth to the sun. This rotation corresponding to one 24-h interval. However, the light intensity which falls on a specific location is not constant, and to determine the "average" daily value, the sunlight over 1 year is factored to determine the daily flux. Under these conditions, 1 year is 365 97/400 days, with January 1st, February 1st, and December 31st representing the 1st, 32nd and 365th day of the year. The highest flux (perihelion) would be when the sun and earth are the closest, and this is approximately the 3rd of January (2016, 2018, 2019, and 2021, and the 5th of 2017, 2020, and 2022), but the dates can differ by a day depending on the position facing away or towards the sun and the position of the moon relative to the earth.

The Earth's orbit around the sun is approximately circular. The minimum and maximum distance from the sun do not differ by more than three million miles (3%); a more significant influence on sunlight is the earth's axial tilt (23.4° on its vertical axis,

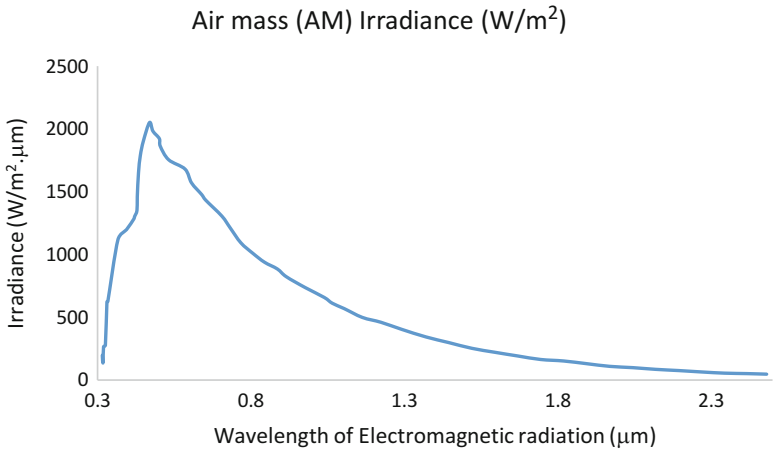

Fig. 1.4 Approximation of dependence of surface irradiance to air mass and wavelength of electromagnetic (EM) irradiance. (Sources: [21, 22])

eccentricity of less than 0.02) that determines the seasons, as the earth tilts towards/away from the sun (summer or winter solstices) or direction of the tilt and the direction to the Sun are perpendicular (equinoxes, Vernal & Autumnal) seasons [23].

The Earth receives a fraction of the possible irradiance of the sun, as it has a smaller cross section ($\pi \times R_E^2$) and tilt cosine angle (θ), which would correspond to approximately 340 W/m^2. As orbital eccentricity increases, the solar irradiance difference becomes significant. The planets Mercury, Mars, and Pluto show significant eccentricity, and therefore there is a magnitude of difference between solar irradiances (2.15-1.36-0.34 respectively relative to $R_E = 1.00$), whereas the other planets show less eccentricity and the ratio of highest and lowest solar irradiance is similar (0.96 (Venus, lowest) −1.16 (Saturn, highest), relative to $R_E = 1.00$) [24].

The spectrum of light from the sun resembles Blackbody radiation (5800 K) of which one-half is in the visible spectrum of the electromagnetic spectrum. The ultraviolet (UV) component of light which is mainly absorbed by ozone can further be classified by the wavelength band which corresponds to "short," "intermediate," and "long" UV wavelengths. These correspond to band "C" (100–280 nm); "B" (280–315 nm); and "A" (315–400 nm). Sunlight comprising of UV radiation has wavelengths which can reach the surface of the Earth (7%). The UV radiation has sufficient energy to promote radical formation and bond weakening in deoxyribonucleic acid (DNA). All major lifeforms on Earth (bacteria, archaea, and eukaryotes) possess DNA and are susceptible to its harmful effects; fortunately, the level of UV radiation exposure at the surface is not high enough to cause permanent damage without prolonged exposure. Wavelengths of lesser photon energy are visible light, infrared (IR, 750–1×106 nm), microwave, and radio wave of which visible light (400–750 nm, 46%) are the main sources of solar radiation for heating and energy. Longer wavelengths past visible light include infrared (IR) radiation and are also classified by wavelength band. IR bands "A" (700–1400 nm), "B"

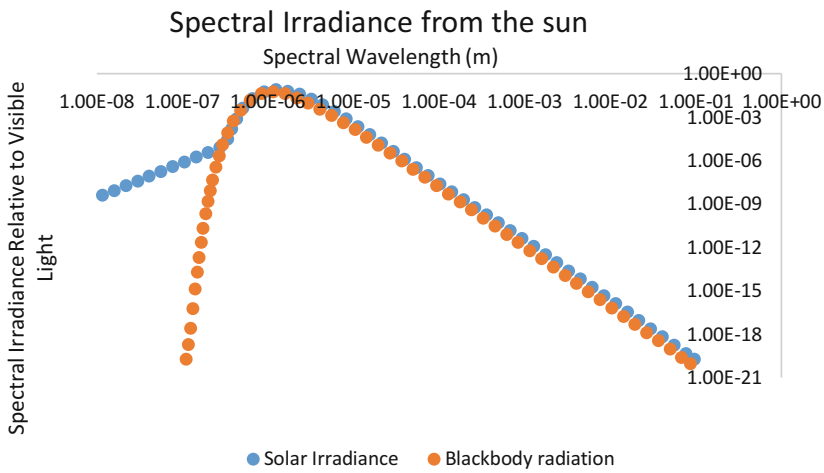

Fig. 1.5 Summary of electromagnetic radiation from the sun and from a blackbody versus wavelength. (Sources: [25, 26])

(1400–3000 nm), and "C" (3000 nm – 1 mm) are used for solar heating (47%). Other bands such as radio waves are too low in energy to be of use. A plot of the EM irradiance from the sun and energy emitted by a "blackbody" having a surface temperature (approximately 5800 Kelvin) is also shown. For practical purposes, most of "useful energy" falls in the visible to infrared wavelength of light, summarized in Figs. 1.3c and 1.5.

While the approximate irradiance is around 1.3 kW/m^2, not all of the irradiance is utilized for heat or electrical current generation due to reflection, absorption, and scattering. As the volume of air becomes greater (air mass, AM), the fraction of useful light reaching the surface diminishes; at its zenith the irradiance is around 1.3 kW/m^2, but as the sun arcs along the sky, the degree of useful light diminishes (e.g., is ~900 W/m^2 at AM1 and ~230 W/m^2 at AM10) as well as latitude (30° "belt") and season (20% lower in the winter relative to the summer).

Solar technologies can be passive or active. In passive, the orientation of the building, water container, and windows relative to sunlight promotes illumination and heating, whereas active utilize sunlight to generate electricity or reactive oxygen species for disinfection or thermal storage for water heating. Even if 1% of available sunlight was used for energy generation, this would be 70-fold more than the entire global energy demand in 2005 [27].

1.3 Solar Thermal Electricity (STE) and Solar Photovoltaics (PV)

Sunlight can be used to boil water to generate steam, which in turn can be used to generate electricity. In addition, photons can be converted to electrons using semiconductors to generate electricity. Thin film silica wafers are used as photovoltaic

surfaces with microcrystalline and amorphous structures. Amorphous silicon has a band gap of 1.7 eV, whereas crystalline silicon has a band gap of 1.1 eV [28]. These bands gaps reflect the ability to absorb different parts of the EM spectrum. Although these cells have lower efficiencies (6%), their greater usage has increased global electricity generating capacity. Global solar capacity in 2035 is expected to be 150% greater than the BP Energy analysis due to falling costs and stronger policy support in China and India, two of the largest solar markets [5]. The average irradiance of 7 kWh/m^2/day can be utilized by heating or photovoltaic systems, which couple the collector to solar arrays that generate direct current (DC). Typically an inverter is used to convert the DC to alternating current (AC) to be used in the general electrical grid [29]. Taking the EIA estimates, it appears that solar PV will become significant in the electricity generation sector in 2030, with wind as a significant provider of US electricity, providing 160 GW by 2050 (relative to 40 GW in 2020, with wind energy proving a constant 120 GW over the 2020–2050 time period), making up 48% of the world's installed capacity and 33% of electricity generation by 2040. In 2017, solar and wind global electricity generation was 1447 TW/h out of 24,860 TW/h or 5.8%; in 2040, it is anticipated to be 12,461 TW/h out of 37,510 TW/h or 33.2% [3].

While Solar PV array capacity factors operate below 25% efficiency, relative to fossil fuel–based power stations (36% Carnot cycle efficiency), their cost per kilowatt is similar, and unlike for fossil fuels, costs are falling for solar PV [30]. In addition, solar panels can be installed as thin film cell integrated to a flexible polymer roofing membrane, or as roof tiles or shingles, to facades of building exteriors, glazing or semi-transparent glass windows, and skylights. The "levelized cost of energy" is a measure of US cents per kilowatt-hour of electricity generated. Fossil fuel-derived energy in the form of conventional and advanced natural gas combined-cycle entering service in 2017 with appropriate tax credits are by 2040 anticipated to generate energy at $53/MWh (at 2017 $ value), while energy from advanced combustion turbine is anticipated to cost around $85/MWh and energy from coal with 30% carbon capture and sequestration at $114/MWh. Energy generation from renewables such as advanced nuclear is estimated to cost around $78/MWh; for biomass $85/MWh; and for onshore wind, at $50/MWh; while offshore wind is anticipated to cost $111/MWh, due to the greater infrastructure costs. Traditional renewables such as geothermal the anticipated cost are $45/MWh; hydroelectric at $58/MWh, while the solar thermal cost is anticipated at $132/MWh and solar PV at $48/MWh. As the earlier cost list highlights, energy production is highly sensitive to the type of fuel and the method employed to generate energy. Using $52/MWh as a benchmark, only advanced combined-cycle turbines, using fossil fuels or renewable fuels such as geothermal, wind, onshore, and solar PV are price-competitive with geothermal being the "cheapest" and solar PV being the most "expensive" within the select energy resources [31]. These capacity-weighted averages also incorporated current costs with available tax credits that are not uniform across all energy mixes, capacities, and efficiencies.

The energy returned on energy invested is a net balance of energy utilized in the construction and operation of an energy resource including environmental impact. The carbon dioxide per kilowatt-hour of electricity varies depending on the system but is generally greater than 15 g/kWh for solar PV over its operating lifetime and is

lower than coal-fired power stations (915 g/kWh), nuclear (6 g/kWh), or wind (11 g/kWh). Heavy metals used as dopants or in cadmium telluride solar cells (CdTe) are toxic (5 g/m^2, 0.3–0.9 μg/kWh over its operating lifetime). Life-cycle cadmium emissions from coal are 3.1 μg/kWh, lignite 6.2 and natural gas 0.2 μg/kWh [32]. The time period before the investment costs are recouped is also different on technology type and varies between 1.5 and 11 years for different types of solar PV systems, assuming a 30-year operating lifetime [33]. The lifecycle analysis also factors in carbon dioxide obtained in the crystallization process:

$$SiO_2(s) + C \rightarrow Si(s) + CO_2(g),$$

Therefore, one mole of silicon will generate 1.5 moles of carbon dioxide at 1700° requiring energy. Approximately 13 MWh of electricity is used to produce 1 t of pure silicon. Approximately 50 tons (tn) of pure silicon ($84,500 per tn) is required to meet the global energy requirements in 2005, and this was approximately 1/100th of the global production of silicon. The harvested silica is used for direct heating of homes, roof solar water heating, solar furnaces, and a sun-concentrated solar thermal power plant. The efficiency of light collection to electricity production is on par with photosynthesis (6–12%). In photosynthesis, light, carbon dioxide, and water are used to generate sugars ($C_6H_{12}O_6$, known as biomass); however, unlike photosynthesis, photovoltaics (PV) cannot alone meet expected demand nor decarbonize electricity generation without input from other renewables. These above physical constraints of silicon process to "commercial grade silicon," cost of energy, and carbon dioxide emission limit the percent mix of solar towards global energy, and it will never meet 100% of the requirement, due to the low production of pure silicon and the energy-intensive processes required; however, solar PV can be a significant contributor towards sustainable energy alongside wind, geothermal, biomass, and nuclear [34].

The energy flow (exergy) and energy efficiency are related to light irradiance which is captured to varying degrees of success by different solar collector designs. In a semiconductor, the valence band is where the electrons are located and the conduction band is where the electrons end up separated by a band gap. The magnitude of this gap will reflect if the material exhibits more conductor-like or insulator-like properties and the spectrum of light that is absorbed [35].

Silicon is a group IV element having four valence electrons, which can be excited by a specific quantum of sunlight (1.12 eV); however, in a semiconductor to facilitate electron movement, the element is doped with electron-rich (group 5, 6, 7) and electron-deficient (group 1, 2, or 3) elements [36]. This creates a potential for electrons to migrate from the electron-rich areas to "holes" in the electron-deficient area, as silicon requires four electrons [37]. This can create positive and negative types which meet at the PN junction and forms the PV cell, with a light receiving antenna at the N-type of the device, illustrated in Fig. 1.6 [38].

The photovoltaic module charge controlled the inverter and storage battery. The photovoltaic module consists of photovoltaic cells which absorb light and generate electricity. The inverter converts direct current to alternating current and the charge controller prevents the battery from being overcharged or discharged to increase

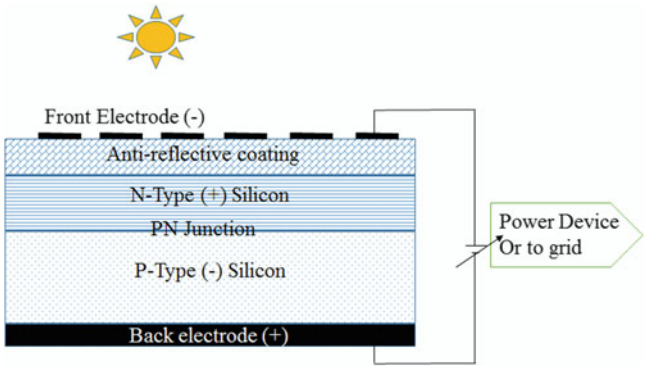

Fig. 1.6 Schematic of Si-based PV cell. (Source: [39, 40])

battery life. Lastly, the battery stores the surplus current. The most common type of solar cells are based on crystalline simplified silicon (sc-Si) or multi-crystalline silicon (mc-Si), thin-film micro amorphous silicon (a-Si), cadmium telluride (CdTe), copper indium selenide (CIS), and copper indium gallium selenide (CIGS) [41]. Recent advances have included organic photovoltaics based on carbon polymers. The above category of semiconductors has band gaps between 1.1 and 1.7 eV [42]. The most common are silicon-based cells that have a band gap of 1.12 eV and are between 11% and 20% efficient, where single silicon crystals are cured by the Czochralski process [43]. In recent years, manufacturers have moved towards thin-film cells that utilized 99% less material than crystalline solar cells, with a light efficiency of 12% and a service life of 25–30 years [44]. The major components are based on either a-Si, CdTe, CIS, or CIGS. The films convert 5–13% of light to electricity [45]. Researches to increase the solar efficiencies of silicon-based solar cells have incorporated hybrid perovskite ($(CH_3NH_3)PbI_3$), organic materials, nanotubes, graphenes, and quantum dots [46].

Moving from inorganic to organic systems offers advantages in terms of flexibility and panel area as well as fabrication [47]. The light absorbing layer is sandwiched between a glass coated with semitransparent indium tin oxide (ITO) on top and a conducting layer underneath (e.g., Al electrode) and a mixture of two ionomers such as poly(3,4-ethylene dioxythiophene) [PEDOT] polystyrene sulfonate [PSS] as a conducting polymer [48]. The wide band gap of 2 eV limits the spectrum of EM radiation that can be absorbed and the overall cell efficiency [49] with graphene support to extend efficiency and absorption range [50]. Other types of solar cells include dye-sensitized cells.

In a dye-sensitized cell, the absorption of light is separated from the transport of charge carriers. The "front electrode" can be thought of glass with transparent conductive tin oxide (TCO), with nanocrystalline titania adjacent to the TCO later separated by a conducting counter electrode. In between the titania and the counter electrode is the electrolyte where the redox chemistries occur. The electrons are fed into this redox cycle by the counter electrode and channeled to the titania, where

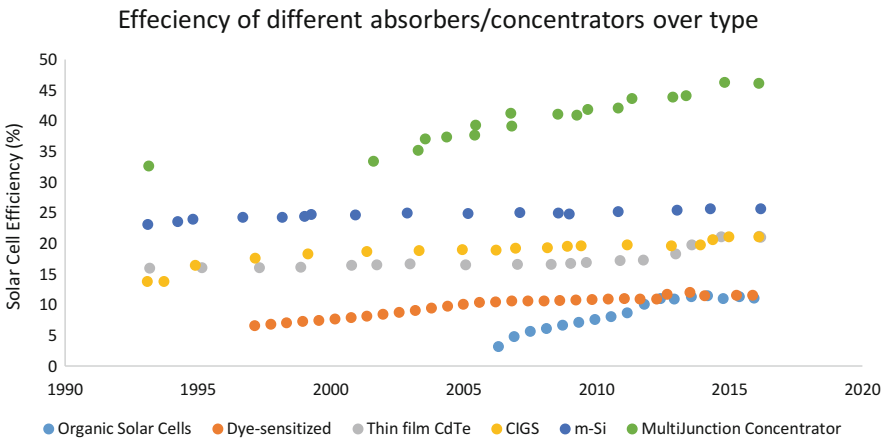

Fig. 1.7 Summary of improving light absorption efficiency of different solar cell/concentrator types of the last three decades. (Sources: [6, 55])

electron transport can occur [51]. This simplified design limits the efficiencies to 7–11% [52]. Other dyes such as ruthenium and zinc complexes have also been used, increasing efficiency with cost. Recently semiconductors such as perovskite-based trialkyl lead halides as light absorption materials have been used and can be 20% efficient [53]. Other areas have focused on metal-free organic dyes based on coumarin, quinoline, or indolines [54]. The differing design and solar cell/concentrator efficiencies are summarized in Fig. 1.7.

Factors that affect solar cell efficiency include surface temperature, solar irradiance, and intermittency, and clouds or dust. This, in turn, affects the cost of kilowatt/hour and has dropped almost 100-fold over the last three decades resulting in lower carbon dioxide emissions relative to coal-fired power stations [56]. A trend appears to be a migration away from silicon towards a-Si, CdTe, or CIGS and organic solar cells, due to their faster payback cycle and wider usage of solar in areas of lighting, water pumping, desalination, and communication [57].

1.4 Solar Cell Primer

Upon absorption of light, electrons are excited to higher orbitals and decay back to their initial states, generating heat but not causing bond cleavage. In electromagnetic radiation, a photon at higher energy, such as in the ultraviolet, can be used to promote bond cleavage. Upon absorption of light energy, an electron residing in a chemical bond may be promoted to a higher vacant orbital creating a “hole” that is “positively” charged [58]. An electron in the conduction band is, therefore, “free” to move within the crystal generating current. Similarly, hole (or charge carriers) can move by sequential “filling” from adjacent electron, which creates a new “hole” in their former location. The movement of charge carriers is related to temperature and band gap of the material.

For a cell to generate current, a circuit needs to be completed in the "opposite" direction to the movement of electrons. A potential barrier selectively separates the two charge carriers that are generated using light energy. The charge separation sets up a voltage difference between the ends of the cell which is used to drive an electric current in an external circuit [59]. To construct a cell, a positive and a negative terminals need to be constructed, and this may be accomplished through selective doping of the silicon crystal. By incorporating an atom with one additional electron relative to Si, such as P, a negative carrier is introduced and the "additional" electron can be used in the crystal's conduction band to form part of an electric current [60].

In addition to the donor dopant atom, an acceptor dopant or positive carrier is also required. The acceptor has one less electron than Si (e.g. B) and would generate a hole. Connecting both n-type and p-type materials at an np junction would enable the charge carriers to migrate in opposite directions. As they move, an "intrinsic" barrier is setup limiting the total number that can migrate and form electron-hole pairs (Fig. 1.8a). Since light irradiance on the surface promotes charge separation, an excess of electrons

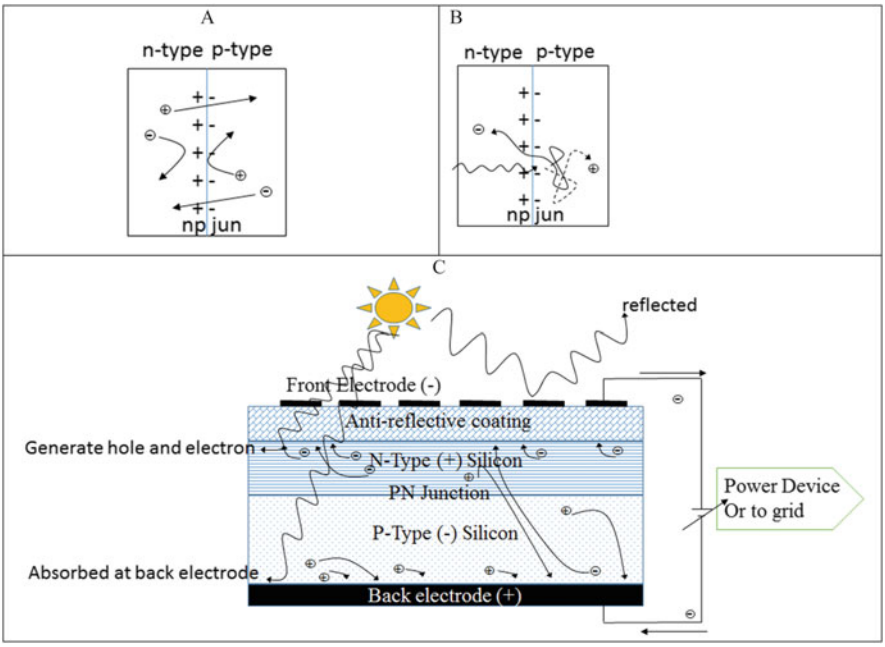

Fig. 1.8 Schematic of a solar cell. (**a**) During junction, electrons move from the n-type Si to p-type, while holes move in the counter direction. The movement of charge carriers in Si builds up an intrinsic barrier at the junction (np-jun) inhibiting further movement of free charge carriers and creates an equilibrium. (**b**) Upon absorption of a quantum of energy, an electron is excited on the p-type of Si and migrates across the np junction (np-jun) before it can recombine with a hole. (**c**) Light irradiance and absorption yields (electron-hole pairs) charge carriers that migrate in opposite direction, separated by the potential barrier, generating a voltage that drives a current through an external circuit from which useful work is undertaken. Some light is lost through reflection or absorbed from the back electrode. (Sources: [39, 40, 64–68])

(on n-side) and holes (on p-side) is generated, creating a charge imbalance in the cell (Fig. 1.8b). Negative charges flow out of the electrode on the n-type side through a load and perform useful work (Fig. 1.8c). The electrons flow into the p-type side, where they recombine with holes [61]. Thus light energy absorbed by the electrons is consumed during electron migration across the external circuit, generating an equilibrium between incident light which creates electron-hole pairs generating a charge imbalance and the PN junction and external circuit which facilitate movement and useful work at the expense of giving up the initially absorbed energy [62]. The incident light is used to generate charge carriers that move in opposite directions across the junction, creating a charge imbalance to drive a current through a circuit [63].

A number of phenomena lead to energy processes that do not lead to useful work. A major source of cell inefficiencies is a loss of light by reflection, ignoring latitude and seasonal changes. Approximately 5% of light is lost through coating the glass to minimize losses through reflection. Light of energies other than that required for excitation of electrons is also not efficiently utilized. Therefore a "useful" material is a material whose valance and conductance bands are separated by less than 2.6 electron-volts (eV) of energy. This corresponds to energy accessible in the visible wavelength spectrum of compatible materials including pure silicon (Si) and the semiconductor gallium arsenide (GaAs). Pure Si has a bandgap of 1.1 eV while that of GaAs is 1.4 eV. Quanta of energies equivalent between 1 and 2.6 eV will promote electrons from the valence to conduction bands and thereby potentially contribute towards energy production. Other factors are direct and indirect electron-hole recombination. The free charge carrier energy can be reduced through collisions, leading to lower charge mobility and lesser current (Fig. 1.9a). These may be related to surface inhomogeneities related to the Si and dopants (Fig. 1.9b). The flow of electrons and holes is related to the resistance of the material summarized using Ohm's law ($R = V/I$) but is not true for materials where recombination losses are not proportional to resistance. Resistance occurs in the bulk of the material, top-surface of the material, and at the interface between the cell and electrical contacts leading to the external circuit (Fig. 1.9c). At higher temperatures, electrons have more energy, but the lattice vibrations also increase and interfere with charge carriers; the increase in temperature lowers the barrier at the junction to separate charges, which for Si occurs around 300 °C (Fig. 1.9d) where thermally excited ions undergo collisions and reduced ion mobility. Resistance losses can be offset through higher doping, at the expense of increased lattice inhomogeneities leading to an excess of free carriers which can overcome the potential barrier at the junction and eliminate any charge imbalance and the ability to generate current in the external circuit.

In the area of solar thermal, concentrated solar thermal are used for heating and concentrated solar power for the generation of electricity, where high magnification mirrors concentrate solar energy to heat to generate steam from water and electricity from steam-driven generators. The designs are parabolic troughs to focus light and heat into a receiver and Fresnel-type mirrors to focus onto receiver tube, towers that are an array of small mirrors which track the sunlight and focus the energy to a specific point, and solar dish collectors that focus light above a reflector dish. The strengths and weaknesses of these designs are summarized in Table 1.1.

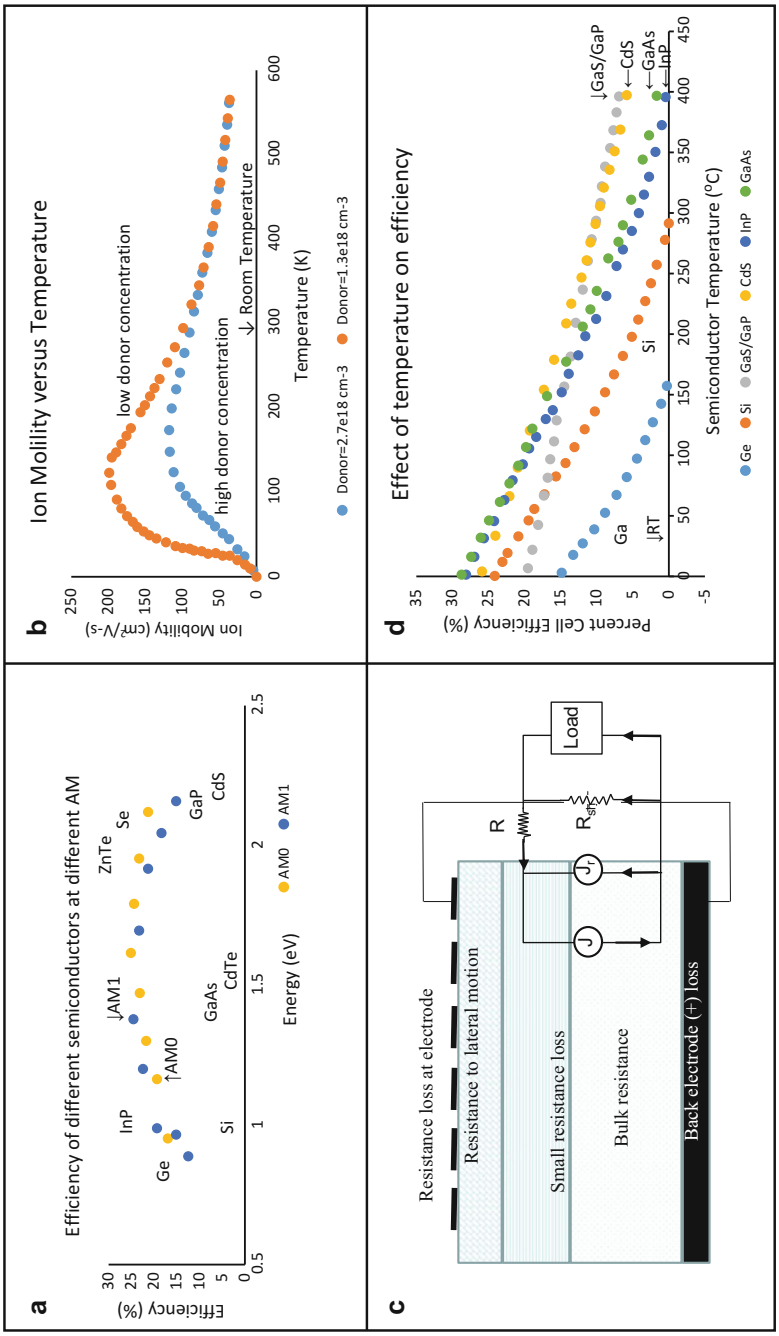

Fig. 1.9 Summary of effects which lead to cell inefficiencies related to (**a**) different semiconductor materials and light absorption at different air mass; (**b**) the effect of donor concentration on ion mobility; (**c**) intrinsic and bulk factors contributing to resistance within the device and circuit; and (**d**) effect of semiconductor temperature on cell inefficiencies. (Sources: [39, 40, 69–73]; Russell 2018)

Table 1.1 Summary of concentrating solar power technologies [74]

Parameter	Parabolic trough	Solar tower	Linear Fresnel	Dish-Stirling
Maturity	High	Intermediate	Intermediate	Low
Operating temperature (°C)	290–550	250–650	250–390	550–750
Max efficiency (%)	20	35	18	30
Max electricity efficiency (%)	16	20	13	25
"Engine"	Superheated steam Rankine	Superheated steam Rankine	Saturated steam Rankine	Stirling
Assembly	Absorber attached to collector and moves with collector	External surface with a fixed receiver	Fixed absorber with a secondary reflector	Absorber attached to a collector, and moves with collector
Storage system	Two-tank molten salt at 380 °C or 550 °C	Two-tank molten salt at 550 °C	Pressurized steam storage (<10 min)	Storage under development
Steam conditions (°C/bar)	380–540/100	540/100–160	260/50	N/A
Capacity/h	7	10	< 7	< 7

Solar energy by 2020 will be available, economic, and competitive with natural gas for heating and coal for generation of electricity in dollar-per-British thermal unit or dollar-per-kilowatt/hour, respectively, particularly be mimicking some design elements from photosynthetic plant apparatus [75] or through incorporation of molybdenum disulfide flakes (MoS_2) into an active buffer layer [76] to extend efficiencies beyond 25% [77] and sixfold increase from the first introduction of perovskite solar cells over the last decade [78] with the potential of semi-transparent solar cells as windows which transmit visible light and utilize IR light for energy [77]. By incorporating flexible hole transporting agents such as 3, 4-ethylenedioxythiophene, efficiencies can be increased [79]. Other approaches to increase efficiency have incorporated tungsten and alumina layers to absorb a wider spectrum of electromagnetic radiation [80], or biopolymers based on chitosan [81], or careful adjustment of redox centers in dye-sensitized solar cells [82]. The major materials will remain Si/CdTe between now and at least 2040 (Fig. 1.10) with other materials becoming significant.

Current solar technology primarily focuses on improvement of absorption to the generation of energy efficiencies, with c-Si as the dominant material. Although Si itself is not a limiting material, the other metals potentially can be limited, requiring recycling of silver, indium, gallium, and germanium which have considerable value.

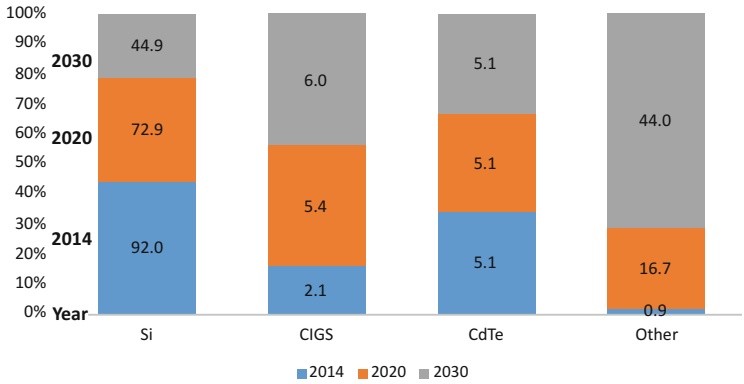

Fig. 1.10 Projected and actual market share of solar panels based on Si, CdTe materials. (Source: [83])

The current recycling technologies also generate energy and utilize harmful solvents, which in turn need to be captured, condensed, distilled, and purified. Currently, few policies cover the entire lifecycle and take account end-of-life scenarios after 25 years of estimated usage. For example, China, India, European Union, and the United States, the dominant regions for solar energy, do not have government-level policies on recycling, nor are the effects of disposal of solar panels in landfills known. In view of the increasing use of solar for the generation of energy (thermal and electrical), the effects of disposal of materials are not undertaken except in a few studies.

1.5 Toxicological Evaluation

Titania (TiO_2) is a common material in DSSC solar cells, as well as an additive in cosmetics and sunscreens and a nano disinfectant [84]. Titania has three geometric forms with rutile (space group: P42/mnm, bulk density 0.04–0.41 g/mL, specific area 130–190 m^2/g) [85] being the most abundant in optical applications [86]. The anatase form (space group: I41/amd, bulk density 0.04–0.06 g/mL, specific area 45–55 m^2/g) [87] is used in organic photovoltaics as an electron collecting layer catalyst, while the Brookite (space group: Pbca, bulk density 0.06–0.10 g/mL, specific area 150–400 m^2/g) [88]. Brookite form has limited commercial usage. The disposal of devices such as solar cells containing titania into landfills often leads to leaching of these ions into the water table, streams, or lakes. While the concentration of leaches is unknown, it is estimated to be less than 1 parts-per-million (ppm) [89]. Previously it was reported that 0.05–1.0 ppm of titania and alumina were toxic to algae over 72 h [90] and did not affect chromium Cr (VI) ion toxicity which increased in a dose-dependent manner [91]. The general observations from the literature are that titania (morphology undefined) or anatase/rutile (4.5:1 c/c) lowers the population of freshwater algae at losses as low as 1 ppm, due to membrane

damage resulting from reactive oxygen species (ROS)–induced membrane weakening [92]. In other studies, it was reported that titania under ultraviolet A radiation was detrimental to algae relative to algae with titania but non-irradiated, presumably due to UV-A–assisted photocatalysis of TiO_2 generating ROS [93]. Since titania has three allotropes with anatase and rutile being the most abundant, it has been demonstrated that the anatase phase is more cytotoxic to mouse keratinocyte than the rutile form. It has also been demonstrated that while both forms are toxic, the mode of action is different. The rutile form initiates apoptosis via ROS, whereas the anatase (P25 type) forms initiate cell necrosis and membrane disassembly [94].

To evaluate the photocatalysis of titania, UV-A, UV-B, and UV-C have been evaluated, with titania with UV-C irradiation being the most toxic to microalgae than only UV-C exposure, as well as human skin fibroblasts. Solar panels also have silver metal–based contacts [95].

In a study silver and titania nanoparticles were investigated on ciliated protozoans, and it was shown that the cytotoxicity was greater with both materials than either one alone (additivity or potentiation) [95]. The effective dose at 50% lethality of titania to *Chlorella* sp. was determined to be 3.36 g/L for the anatase (25 nm nanoparticles) form and 6.26 mg/L for the rutile (10 nm diameter × 40 nm length rods) form under UV irradiation at 72 h exposure. The reduction in chlorophyll was 31.6% for the anatase form and 29.76% for the rutile form. Surprisingly, additive (same direction) and antagonistic (opposite direction) responses were also found when both forms were co-mixed in varying mixtures. The 0.25, 0.25 mg/L and 0.5, 0.5 mg/L were antagonistic, whereas the 1, 1 mg/L was additive when chlorophyll yield was measured. For example, titania uptakes into the algal cells varied as a function of dose and type. At 0.5 mg/L concentration, there was approximately 25% (± 5%) update of the anatase form; for rutile form, the uptake was almost 80% (± 1%), and for the combined (0.5:0.5 c/c) anatase:rutile, the update was almost 60% (± 30%) [96]. The toxic effects of titania and other metal ions on bacteria or tissue are dependent on the ionic charge and the type of metal, as well as mode of toxicity [97]. In general metal ions such as silver (Ag^{+}), zinc (Zn^{2+}), and mercury (Hg^{2+}) [98] demonstrate strong cytotoxicity at 11 ppm (Hg and Ag) and 16 ppm (Cu). Cobalt (Co^{3+}) demonstrates intermediate cytotoxicity in human tissues but not in microorganisms; aluminum (Al^{3+}) exhibits no toxicity to either human tissues or microorganisms [99]. Thus metals that can behave as disinfectants are limited to Cu^{2+}, Ag^{+}, and TiO_2. Human osteoblast-like (MC3T3-E1) cells appear to be tolerant to titania (Ti6Al4V) alloy including titania doped with copper (4xCu-TiO_2) [100].

The most common mechanism for toxicity is intracellular ROS production, triggering of antioxidative and inflammatory gene expression in a concentration-dependent and time-dependent manner. For example, Si nanoparticles are cytotoxic and initiate inflammatory response through increased expression in cyclooxygenase-2 (COX-2), tumor necrosis factor alpha (TNF-α), interleukin 1 beta (IL-1β), interleukin-5 (IL-5), and interleukin-8 (IL-8) which is distinct to iron (Fe^{3+}) and titania which do not induce broad array of inflammatory mediators. TNF-α mRNA levels in adenocarcinomic human alveolar basal epithelial cells (A549) and inducible nitric oxide synthase (iNOS) in macrophages were elevated [101]. The levels of ROS

and cytotoxicity or degree of inflammation does not positively correspond, suggesting a distinct biochemical signaling mechanism. Titania, for example, will increase ROS without increased cytotoxicity. Bio-coating of silica with serum proteins would eliminate their inflammatory and cytotoxicity potential. The murine macrophage cell line RAW264 exhibited delayed toxicity upon incubation with Si which was detected after 72 h exposure with a slight increase in ROS [102]. Titania nanoparticles were not found to be toxic in the same cell line, but increased ROS levels and induced TNF-α expression and detection of macrophage inflammatory protein II (MIP-2) were detected [103]. Titania induced enhanced ROS and DNA damage [104], but at 300 ppm did induce interleukin-8 expression in A549 cells [105]. While effects at a high dose may be observed within 24 h, lower doses, such as 50 ppm, may exhibit a response at 72–96 h time period in A549 cell [106]. The mechanism by which titania is taken into the cell is via passive diffusion, active transport, and phagocytosis and to a lesser degree by clathrin-dependent endocytosis [107], but is highly dependent on nanomaterial morphology, dimension, cell type, media, serum, and incubation time, as well as dose. Incubation between 50 and 400 ppm at 24–168 h has shown toxicity under different experimental conditions. A comparison of Fe^{3+}, $Si^{0,4+}$, and Ti^{4+} has shown that uncoated Si^0 is the most toxic in electing an inflammation response as a result of elevated ROS and activation of other proteins, such as stress-activated protein c-Jun N-terminal kinase (JNK), which result in apoptosis. Induction of inflammatory cytokines like interleukin-6 and interleukin-8 and chemokines by amorphous Si^0 can lead to damage to human lung epithelial cells [108]. Silicon is also known to trigger the release of TNF-α and increased expression of MIP-2 in RAW264.7 macrophages, the response related to the specific surface area of the nanomaterials rather than the diameter [109]. Both titania and silica lead to inflammation in human monocytic (THP-1) cell line and murine macrophages [110] and may be related to the degree of agglomeration rather than initial diameter which in turn affects surface area. Elevated interleukin-8 can also lead to lysosomal damage [110] in a number of different cell systems [111]. The amelioration of the cytotoxicity exhibited by silica after coating suggests that the sites of interaction are phospholipids in the cell membrane, wherein media silica forms silanol intermediate where the negatively charged oxygen [O^-] interact with the positively charged [$'R(^+NCH_3)R$] trimethyl-ammonium head group of the membrane lipid, leading to increased membrane plasticity and unzipping or membrane degradation. Other possible mechanisms include uptake mediated by scavenger receptor (SR-A) as shown in Si uptake in RAW264.7 macrophages [112]. Silica binding to SR-A might trigger p38 kinase downstream and release of TNF-α and inflammation [113].

Titania in primary human dermal fibroblasts (HDF) and human lung carcinoma (A549) cells will facilitate the generation of interleukin-8 which in turn will increase lactate dehydrogenase (LDH) activity, a measure of cytotoxicity. Dose-dependent toxicity was observed at 1500 ppm, which is a much higher dose that observed with carbon (C_{60}) nanoparticles [114] with the phase (and not surface area) being related to toxicity. Here, anatase form (153 m^2/g) was found to induce cytotoxicity, whereas rutile form (123 m^2/g) did not, and mixed forms appeared to be additive in terms of

toxicity. The differences in toxicity might be explained by the degree of hydration and water splitting catalysis by the different titania types. For example, it appears that the anatase phase is able to adsorb dissociatively [115], whereas rutile phases adsorb non-dissociatively [116]. Upon UV radiation, hydroxyl radical is generated on the surface of anatase titania via Ti-OH and OH^- interactions. The hydroxyl ($HO^\bullet$) radical is the primary reactive oxygen species and is able to degrade organic dyes via first-order kinetics. The half-life ($t_{1/2}$) for Congo red degradation by anatase phase titania was 1.5 min,g, whereas it was 120 min for rutile phase and 3.5 min for Degussa formulation (80:20 anatase:rutile) form and not related to differences in surface area. Reactive oxygen species, in turn, lead to cellular damage, such as measured by LDH release (at 1500 ppm in the dark or 30 ppm with UV radiation, whereas the rutile form was not active at any concentrations up to 1500 ppm). Unlike fullerenes (C_{60}), titania can also affect the mitochondria, as examined by the (1-(4,5-dimethylthiazol-2-yl)-3,5-diphenylformazan [MTT]) assay. Mitochondrial toxicity was observed using anatase at 1500 ppm but not rutile. General inflammation by measuring interleukin-8 was also shown to be effective for anatase (at 300 ppm) but not for rutile form, which correlated with the ability of the nanomaterial to generate ROS. Reactive species were observed for anatase but not for rutile and this, in turn, was related to illumination with UV-A for anatase that appeared to potentiate the response but not for rutile [117]. While this study contradicts several other studies in showing no toxicity for rutile form of titania, it is consistent with the general literature which indicates that the toxicity of titania is highly dependent on the type, morphology, concentration, matrix, media, incubation time, and cell type. To weigh the difference between these studies, we investigated the effects of titania without modification and embedded in ceria and their toxicological effects in bacteria.

Cerium oxide (CeO_2) has been used widely used for catalysis because of its high catalytic properties. From the fluorite-type structure of ceria, the catalytic properties and oxide ion conductivity has been originated, and the partial reduction of Ce^{4+} to Ce^{3+} gives rise to oxygen vacancies. Titania (TiO_2) is the chemically stable, environmentally compatible, and functionally versatile oxide materials. The modified material properties and functions of TiO_2 are determined by their nanostructures, which are influenced by many external factors, predominantly pressure, temperature, and the surrounding environment. The nano Tio_2 materials are also having some mechanical properties such as elasticity and deformation behavior. They also have some bulk properties which include a high refractive index and ultraviolet light absorption.

1.6 Photocatalytic Reactivity

The photocatalysis is a process to accelerate a photochemical reaction in the presence of light, which is absorbed by the catalyst. The photo-reactivity is highly dependent on the catalyst reactivity to generate an electron-hole pair. Through the electron-hole pair, free radicals can be generated when a secondary reaction occurs. This photocatalyst is

practically used in water purification, such as removal of pharmaceutical waste. This study uses methylene blue as a model molecule to evaluate the photocatalytic reactivity of TiO_2 nanomaterials, which are the most commonly used semiconductor photocatalyst. The photocatalytic properties of TiO_2 utilized in various environmental applications was investigated in this research.

1.7 Bactericidal Properties

Nanoparticles have various biological applications; they can be used as sensors, for analyte detection, drug targets, pathogen detection, etc. NPs have been employed in sensors for a variety of applications including detecting analytes at very low concentrations, detecting and separating pathogens, detecting and capturing cells, and detecting molecular and cellular functions. By taking the advantage of the unique properties of the nanoparticles such as high surface area, small size, and composition-dependent properties enables the use of surface ligands as a way to amplify the detection threshold or provide more rapid detection. The nanoparticle biosensors are mainly focused on using inorganic materials particularly metal or magnetic nanoparticles. Gold nanoparticles have been used as sensor due to their surface chemistry. TiO_2 has a capability of killing both Gram-positive and Gram-negative bacteria, although Gram-positive bacteria are less sensitive because of their ability to form spores. The concentration of the TiO_2 which is required to kill the bacteria will range from 100 to 1000 ppm depending on their size, intensity, and wavelength of light used. Recent studies indicate that the TiO_2 nanoparticles are able to kill viruses such as Hepatitis B virus, Poliovirus 1, and herpes simplex virus. The antibacterial activity of TiO_2 nanoparticles is related to the production of hydroxyl free and peroxide radicals formed under UV irradiation by the oxidative and reductive pathways. A strong absorbance of UV renders activation of TiO_2 under solar irradiation, significantly enhancing solar disinfection. The inhibitory effect of nanomaterials on the microorganisms such as bacteria is through various processes such as membrane lysis and inhibition of critical proteins (sources of carbon, nitrogen, sulfur, and oxygen) and nucleic acids. They will affect both outer and inner membranes, phospholipid peroxidation, cell wall weakening and lysis, interaction with lipoproteins, Omp carrier proteins and LP in the periplasm resulting in plasma membrane peeling and rupture, as well as DNA fragmentation.

1.7.1 Experimental Procedure

The aim is threefold, for (1) material synthesis of Ce-doped TiO_2 nanoparticles (CTO-NPs) and fabrication variable optimization; (2) characterization of these CTO-NPs; and (3) photocatalytic and biological applications of these CTO-NPs. All chemicals, solvents, and reagents unless otherwise specified were obtained from VWR International (West Chester, PA) or Sigma-Aldrich (St. Louis, MO). Double-distilled, filtered ultrapure water was used (Ultraopure™, Barnstead,

Dubuque, IA, referred to as distilled water) where water-based solvents were necessary, and all solvents were a reagent or high-performance liquid chromatography (HPLC) grade.

1.7.2 Synthesis Overview

In this section, the colloidal and solid-state chemistry was employed to produce CTO colloids and powders. The optimal variables of fabrications were studied.

1.7.3 Colloidal Synthesis

The nanoparticles are fabricated by the sol-gel method, a wet chemical method, which is also called as chemical solution deposition. This process is a series of chemical reactions which irreversibly converts a homogeneous solution of reactant precursors (a sol) into a three-dimensional polymer (a gel) forming an elastic solid as the same volume of the solution. Through this process, uniform in size, fixed shape, crystalline nanoparticles were fabricated with defined optical, magnetic, and physical properties. The procedure of the CTO-NP synthesis and the optimal variables are summarized below (Fig. 1.11):

1. Drop-wise addition of titanium butoxide ($Ti(^{n}OBu)_4$) to 40 mL of isopropanol.
2. Agitation on a magnetic plate at room temperature (RT) for 60 min.
3. Specific mass of cerium oxide nitrate is added to 10 mL of distilled water.
4. After 60 min stirring of the titania slurry, the cerium oxide nitrate stock is added in drops to the TiO_2 and isopropanol mixture.
5. The binary mixture is stirred for an additional 60 min.

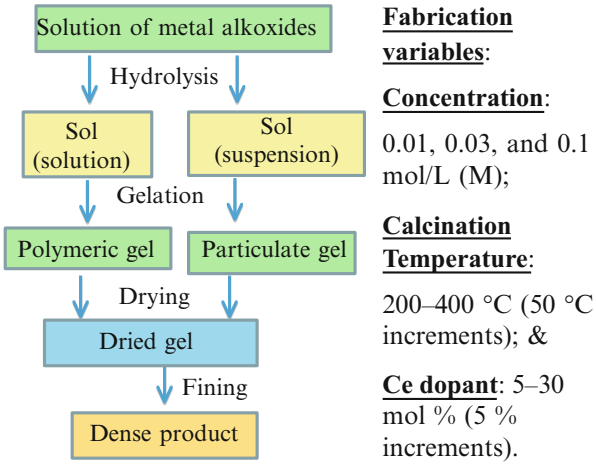

Fig. 1.11 The schematic of the synthesis of CTO-NPs and the key fabrication variables

1.7.4 Solid State Chemistry to Produce CTO-NPs

A solution of titanium butoxide and isopropyl alcohol was mixed and kept under constant stirring for about 45 min at room temperature. The desired weight percentage of 0.05–0.35 (+0.05 increments) of cerium nitrate was mixed with water and this was added to the gelling solution to obtain a doped gel of titania. The solution was then converted to gel, which was calcinated at desired temperatures of 200 °C, 250 °C, 300 °C, 350 °C, 400 °C for 2 h to obtain a powder. A solution of titanium butoxide [$C_{16}H_{36}O_4Ti$] and isopropyl alcohol [C_3H_8O] were mixed and kept under constant stirring for about 45 min at room temperature (also shown in Fig. 1.11). The desired weight percentage (% wt) of 0.05–0.35 (+0.05 increments) of cerium nitrate [$Ce(NO_3)_3$] was mixed with water [H_2O]. This trinary system was mixed for initially forming a gelling solution to obtain a doped gel of titania [TiO_2]. The gel was calcinated at desired temperatures of 200 °C, 250 °C, 300 °C, 350 °C, and 400 °C for 2 h to obtain a white powder.

1.7.5 Characterization of Titania

To evaluate the cerium-doped TiO_2 nanoparticles (CTO-NPs), a series of advanced instrumental techniques was employed to achieve information on morphology, vibration modes, and crystalline structures. X-ray powder diffraction (XRD, Bruker D8 Advantage) was used to collect the crystalline structure and crystallite size (*X-ray powder diffraction*). The electron microscopic analyses, namely transmission electron microscope (TEM, FEI G2-F20) and scanning electron microscopy (SEM, JEOL 6700F), were used to evaluate the crystalline structures and porosity under ultrahigh vacuum (*transmission and scanning electron microscopy*). The spectroscopic analyses, such as ultraviolet-visible spectroscopy (UV-VIS, Beckman Coulter DU 800), were used to determine the functional groups in the CTO-NPs. X-ray energy dispersive spectrometry (EDS) was used to determine the chemical components and elemental composition. The characterization methods and associated technique variables are discussed in the following sections.

1.7.6 X-Ray Powder Diffraction

A Bruker D8 advantage diffractometer equipped with Germanium bent crystal monochromator, using copper radiation ($\lambda = 1.5414$ Å, $K_{\alpha 1}$), was also used to identify the crystalline structure with superior resolution. In the cavity of the glassy sample holder, the specimen is placed and is allowed to be naturally dried. From the diffraction angle range of 20–80°, the XRD patterns were recorded. The data were collected using JOB data collection software and analyzed by Jade 7.0 package. The background was removed and the XRD pattern was indexed with the standard PDF files. The operational variables were controlled at 40 kV and 44 mA. The data collection was carried out at ambient condition.

1.7.7 Transmission and Scanning Electron Microscopy

An FEI Tecnai G^2-F20 transmission electron microscope (TEM) (FEI Company, Hillsboro, Oregon) equipped with X-ray energy dispersive spectrometer (EDS) capabilities was employed to obtain nanostructure information and crystalline phase about the colloid-derived nanoparticles. The instrument was operated in the TEM mode to obtain the high-resolution images of crystals, as well as scanning TEM (STEM) mode. The spherical aberration coefficient and resolution were approximately 2.0 and 0.27 nm, respectively. A probe size of 1 nm was used for EDS. Although a simplification, the collected image contrast is related to the atomic number (Z) squared, with elements with higher Z contributing to brighter contrast. The surface morphology and texture of the crystalline materials were also examined using a JEOL 6701F field emission scanning electron microscope (FESEM, JEOL Ltd., Plano, TX). The surface morphology and texture of the CTO-NPs were also examined by a Quanta 600 FEG field emission scanning electron microscopy (SEM) (FEI Company, Hillsboro, OR). FESEM is capable of generating and collecting high-resolution and low-vacuum images. The FESEM was equipped with a field emission gun and a Schottky emitter. The voltage was controlled at 5 or 15 kV and beam current at 100 nA. The chamber pressure and gun pressure were controlled at 3.5×10^{-5} Torr and 3.0×10^{-9} Torr for high resolution. A thin layer (4.0 nm) of gold (Au) metal was sputtered onto the sample surface to improve conductivity.

1.7.8 Spectroscopic Analyses

Ultraviolet visible spectroscopy: The UV-VIS spectrophotometer (Beckman Coulter, DU 800) is used to measure the optical absorbance spectrum of the synthesized nanoparticles. Deuterium and Tungsten light sources are the main compositions of this spectrophotometer. UV-VIS spectrophotometer is also provided with a grating to filter the selected wavelengths between 190 and 1100 nm spectral bandwidth with less than 1.8 nm bandwidth. The DU acquisition and analysis software for wavelength (RediScan) was used which exports to Excel functionality, with post-processing carried out within Excel. The absorbance spectrum data that is obtained can be tested by estimating it with a Gaussian distribution. The estimation was done using RediScan and Excel software to analyze the data.

X-ray energy dispersive spectroscopy: As stated previously, this EDS is equipped with Quanta 600 FEG field emission scanning electron microscopy (SEM) (FEI Company, Hillsboro, OR). EDS was used to evaluate the elements and their composition based on the principle of emission.

Photocatalytic reactivities of CTO-NPs: Photocatalytic $Ce_xTi_{1-x}O_2$ NPs to decompose MB was tested under visible light and darkness, respectively. The Log reduction analyses were used to determine photocatalytic reactivities of NPs to decompose MB under visible light. $Ce_xTi_{1-x}O_2$ NPs was introduced into the diluted MB aqueous solution and UV-VIS data were collected every hour to estimate the

Table 1.2 Absorbance calibration curve of methylene blue (MB, stock solution: 20 ppm)

NP volume	Concentration of nanoparticles (9500 ppm)	Volume of methylene blue (mL)	Concentration of methylene blue (20 ppm)	Total volume (mL)
9	7500	2	3.6	11
9	750	2	3.6	11
9	75	2	3.6	11
9	7.5	2	3.6	11
9	0.75	2	3.6	11

photocatalytic efficiency of CTO-NPs under visible light and in the dark, respectively. Methylene blue a cationic thiazine dye with molecular weight 319.86 g/mol was further diluted 20 ppm (parts per million). The $Ce_xTi_{1-x}O_2$ NPs with 7500 ppm (0.3 M) were used to test the photocatalytic activity. Serial dilutions of the nanoparticles were made until the concentration became 0.75 ppm as shown in Table 1.2. The MB was diluted from 20 to 3.6 ppm, and this concentration is used to test the photocatalytic activity. The CTO-NPs and methylene blue are mixed in specified volumes as shown in the table below and each sample is tested both under the visible light and in dark with no visible light. Therefore, we can observe the percentage of methylene blue degradation of the samples in both visible light and dark, respectively. Comparative studies can be made by observing the degradation under two different conditions. The samples should be kept under sunlight and the intensity of the light should also be noted. For every 1 h, the samples are tested with UV/Vis spectrophotometer at 200–800 wavelength.

1.7.9 Bactericidal Performance of CTO-NPs

The bactericidal activity assays were performed using *Serratia marcescens (S. marcescens*, commercially available strains ATCC 13880 were used) as the model organism to evaluate the bioactivity of CTO-NPs. Gram-positive bacteria, *Micrococcus luteus* (*M. luteus*, Gram-positive, ATCC 49732) was also used to test the bioactivity of CTO-NPs. Both types of bacteria (5.0 mL) were cultured in Difco™ nutrient LB broth (Miller Luria-Bertani, Becton-Dickinson, Franklin Lakes, NJ) in an incubator shaker (Innova® 43, Incubator Shaker Series, New Brunswick Scientific, NJ) at 37 °C for 24 h. The cultured bacteria were then diluted to 50 mL. The CTO-NPs (0.050 M, 2 mL) were tested against the above bacteria. After the treatment, an aliquot (0.5 mL) was collected and tested using ultraviolet visible spectroscopy to identify the absorbance every hour to determine the optical density (OD) at 600 nm. Control experiments were carried out under identical conditions in the absence of the CTO-NPs, which is used as a disinfectant. In this study, it is defined that no growth of bacteria cells indicates full bactericidal activity and growth indicates partial or no bactericidal activity. Our previous experience in

determining number of colonies per milliliter (CFU) for *bacteria* using dilute samples (abs < 0.6) approximates to 1 OD unit corresponding to10^9 bacteria per mL, therefore OD_{600} is an excellent implicit comparative technique in assessing bacterial viability, whereas plate dilution and counting of colonies is explicit and more accurate where bacterial growth phase is not known or new strains are used for the first time.

1.8 Results

In this chapter, synthesis and characterization of CTO-NPs and their photocatalytic and biological application will be discussed in sections related to the *Synthesis of CTO-NPs, Characterization of CTO-NPs* (*X-ray powder diffraction*, *Spectroscopic analyses*, and *Electron microscopic analyses*), and *Application of Nanomaterials* (*Photocatalytical reactivities* and *Bactericidal performance*), respectively.

1.8.1 Synthesis of CTO-NPs

In this study, sol-gel chemistry was used due to its benefits, such as low processing cost, energy efficiency, high production rate, rapid productivity of fine homogeneous powder, achievable uniformity at low temperatures, and high purity of the final products. However, this method displays some demerits, for example, large volume shrinkage and cracking during drying.

1.8.2 Characterization of Titania

In this chapter, the instrumentation analyses (X-ray diffraction, electron microscopy, and spectroscopy) were discussed. These methods were used to evaluate the morphological and crystalline structure and elemental composition of the CTO-NPs.

1.8.3 X-Ray Powder Diffraction

X-ray powder diffraction (XRD, Bruker D8 Advantage) was used to collect the crystalline structure and crystallite size. The XRD results (Fig. 1.12) indicated that the CTO-NPs with different formulations were well-indexed with tetragonal anatase TiO_2 structure (PDF 01-086-1157). The lattice constants were 3.7852×9.5139 Å and $90 \times 90°$, respectively. XRD indicated that there is no second phase, suggesting that Ce^{4+} cations replace the Ti in the lattice. This study indicated that dopant of Ce with a lower amount than 0.35 shows no effect on the crystalline structure. However, it is hypothesized that the band gap may be reduced due to the inner transition metal doping from the photocatalytic study.

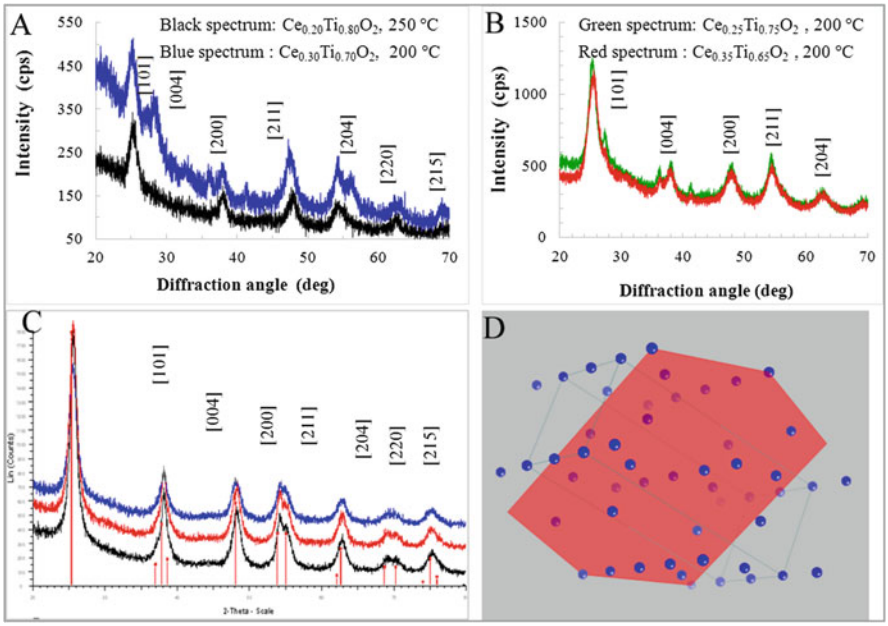

Fig. 1.12 The XRD analyses of CTO-NPs. (**a** and **b**) CTO-NPs with four different formulations (different Ce dopants and calcination temperatures); (**c**) TiO_2 anatase structure as a reference (Liu's previous data); (**d**) Anatase TiO_2 structure

1.8.4 Transmission and Scanning Electron Microscopy

In this study, the transmission electron microscope (TEM, FEI G2-F20) was used to evaluate the morphology and particle size distribution of the CTO-NPs with different doping amounts (Fig. 1.13a, b). TEM images indicate that the fibrous networks were formed. Nanoparticles were found to be agglomerated due to heat treatment, sized at 125 nm. The dark spots were found to be resulting from Ti and Ce heavy elements. Scanning electron microscopy (SEM, JEOL 6700F) was also used to evaluate the morphology of the CTO-NPs (Fig. 1.13). It was found that the charging of samples occurred, due to the existence of organic residue. Coating electronic conductive layer onto the sample surface will remove electrons, further to resolve the charging.

1.8.5 X-Ray Energy Dispersive Spectroscopy

X-ray energy-dispersive spectroscopic (EDS) chemical analyses of three regions (Fig. 1.14) also confirmed Ce and Ti molar ratios were maintained in the final CTO-NPs as experimental design. The principal emission of Ti occurred at

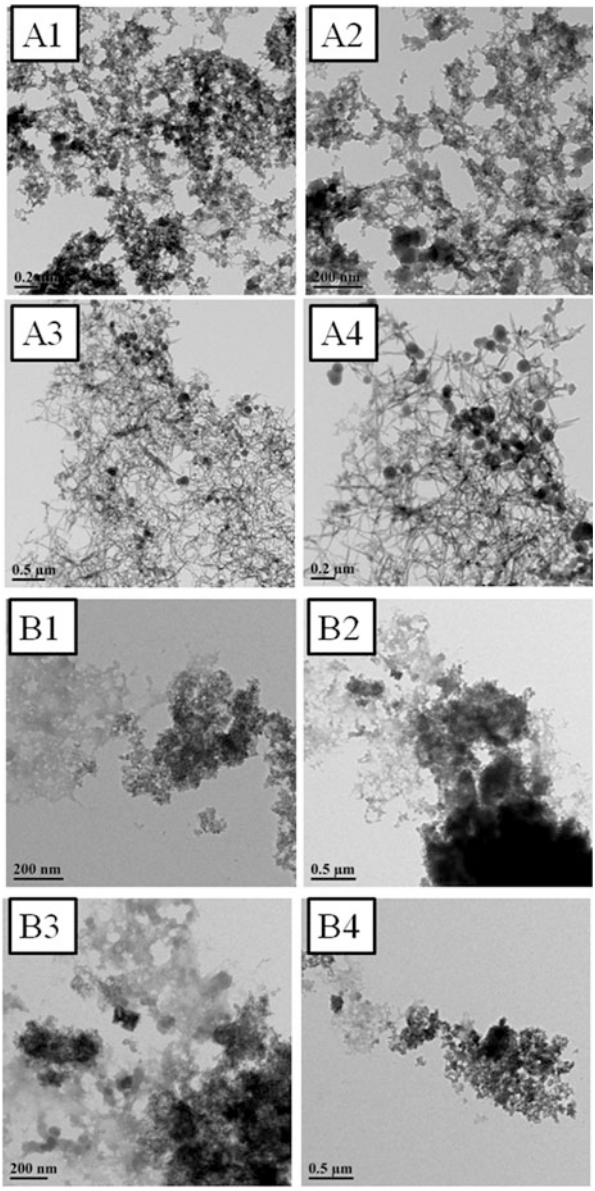

Fig. 1.13 The TEM analyses of CTO-NPs. (**a**) $Ce_{0.35}Ti_{0.65}O_2$ NPs and (**b**) $Ce_{0.30}Ti_{0.70}O_2$ NPs

4.510 keV ($K_{\alpha 1}$) while that of Ce occurred at 4.840 keV ($L_{\alpha 1}$). Two elements Pt and Pd were also observed which result from the conductive coating layers. Figure 1.14a, b are obtained from EDS equipped with TEM and Fig. 1.14c from EDS equipped with SEM. Both analyses confirmed that the Ti and Ce amount totaled at 100%.

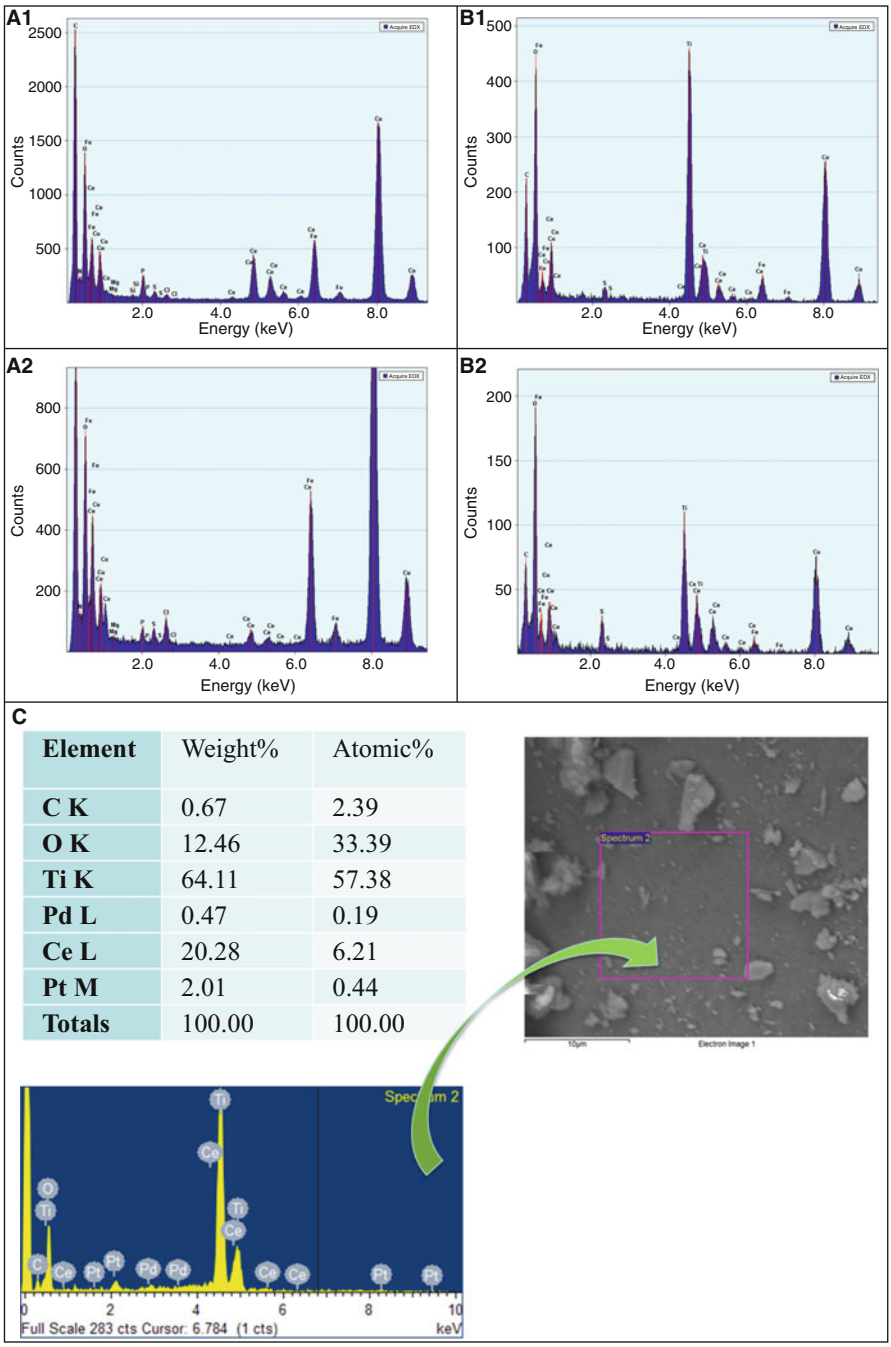

Element	Weight%	Atomic%
C K	0.67	2.39
O K	12.46	33.39
Ti K	64.11	57.38
Pd L	0.47	0.19
Ce L	20.28	6.21
Pt M	2.01	0.44
Totals	100.00	100.00

Fig. 1.14 The EDS analyses of CTO-NPs (equipped with TEM). (**a**) $Ce_{0.35}Ti_{0.65}O_2$ NPs and (**b**) $Ce_{0.30}Ti_{0.70}O_2$ NPs. (**c**) EDS analyses of CTO-NPs, equipped with TEM

1.8.6 Applications of Nanomaterials

The Ce-doped TiO_2 nanoparticles (CTO-NPs) were found to be effective at photocatalyst and disinfectant. This chapter will discuss the photocatalytic reactivity and bactericidal efficacy of CTO-NPs with different formulations, respectively.

1.8.7 Photocatalytical Reactivities of CTO-NPs

Standardization: A methylene blue (MB) dye stock solution was prepared with a concentration of 20 ppm, which is further diluted from 2.4 to 0.4 by using isopropanol as a solvent. The absorbance of these dilutions (Fig. 1.15a) was then measured by using UV-Visible spectroscopy (Fig. 1.15b). It can be observed that the major absorbance peak occurred at 292 nm and 652 nm due to a benzene ring and hetero poly aromatic linkage, respectively. A calibration curve was also plotted using the absorbance of decomposed MB solution as a function of the concentrations. The results showed good linearity of the standard curve was received from the high correlation coefficient (R) (Fig. 1.15c).

Photocatalytical reactivities: A series of methylene blue (MB) decomposition tests were carried out with CTO-NPs. Initially, two concentrations of CTO-NPs were tested, indicating MB decomposition occurs instantaneously at high CTO-NPs

A: concentration dilution

C (ppm)	V of MB (mL)	V of Solvent * (mL)	Total V (mL)
0.4	0.2	9.8	10
0.8	0.4	9.6	10
1.2	0.6	9.4	10
1.6	0.8	9.2	10
2.0	1	9	10
2.4	1.2	8.8	10

* (Isopropanol and water: v/v = 9/1)

A. variables used;
B. 650 nm is used as standard range of MB; and
C. standardization curve.

B: absorbance measurement of MB

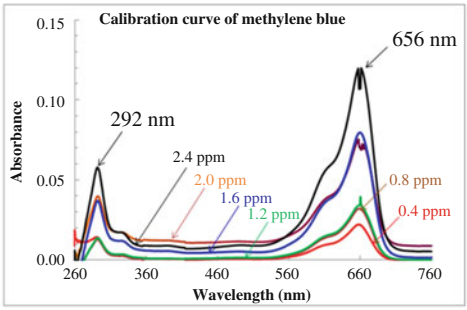

C: stndardization curve of MB

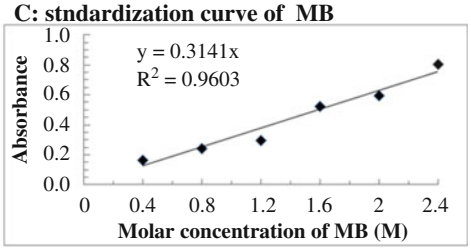

Fig. 1.15 Absorbance calibration curve of methylene blue (MB, stock solution: 20 ppm), (**a**) different dilutions of MB solution; (**b**) absorbance of the MB under decomposition; and (**c**) the standardization curve

concentrations (Fig. 1.16). Therefore, further dilution was carried out from 7500 to 0.75 ppm to determine the lowest concentration of CTO-NPs. The decomposition efficiency was tested under different conditions, namely visible light and darkness. The absorbance was measured at different time intervals 60, 120, and 180 min with UV-VIS spectroscopy (Fig. 1.16b). From the figure, we can see that the methylene blue decomposition rate seems to increase with the increase in the concentration of $Ce_{0.35}Ti_{0.65}O_2$. The Log reduction analyses indicated that MB degradation was catalyzed using CTO-NPs under visible light. The NPs with $Ce_{0.35}Ti_{0.65}O_2$ formulation displayed the highest efficiency compared with another doping amount. It was also found that the lower efficiency of MB degradation in the dark compared with under visible light was as expected.

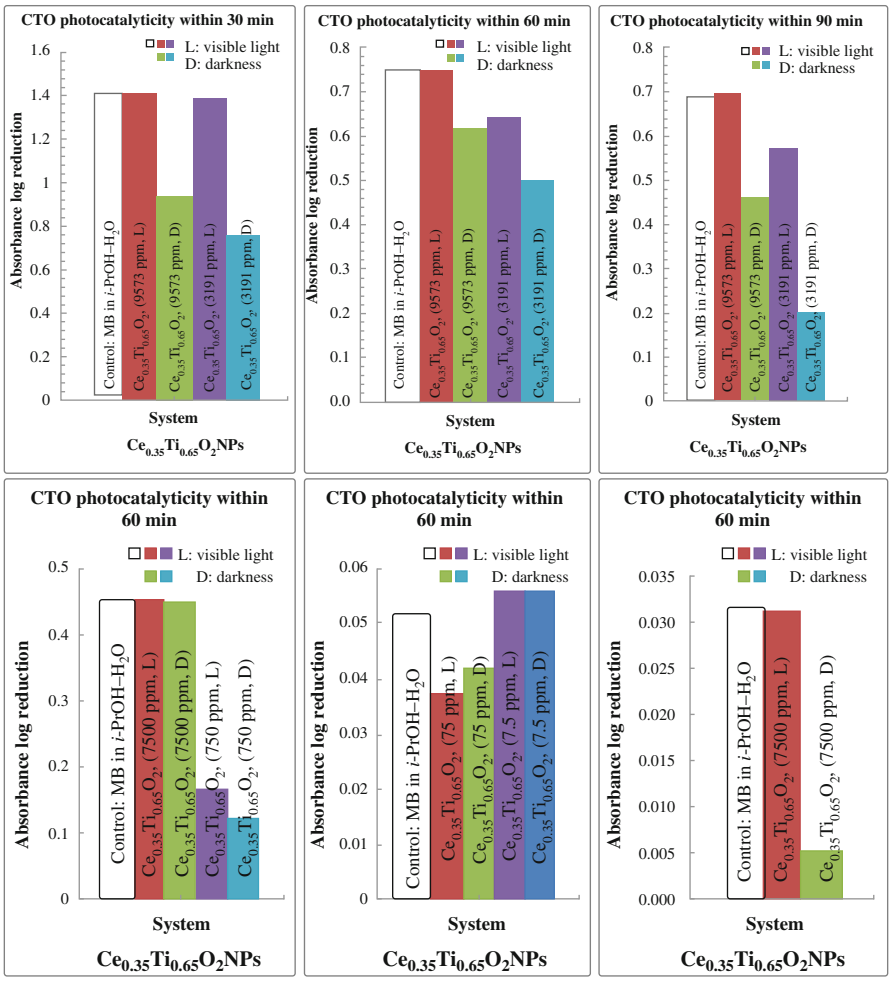

Fig. 1.16 (continued)

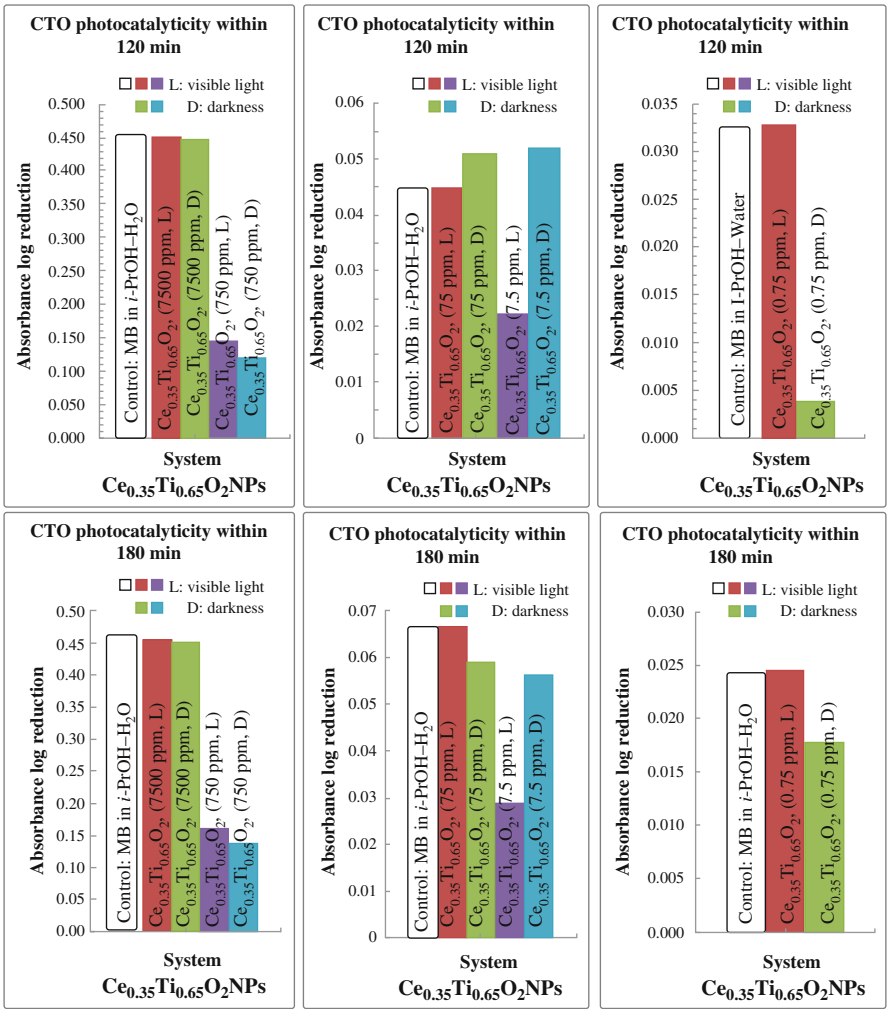

Fig. 1.16 (**a**) The photocatalytic reactivities of CTO-NPs ($x = 0.35$): two different concentrations were tested in either darkness or under visible light, indicating the MB decomposition occurred instantaneously. (**b**) The photocatalytic reactivities of CTO-NPs ($x = 0.35$): diluted concentrations were tested to evaluate the decomposition of MB with a prolonged time period

1.8.8 Bactericidal Performance of CTO-NPs

The bactericidal activity assays were performed using Gram-negative bacteria, *Serratia marcescens (S. marcescens*, commercially available strains ATCC 13880), and Gram-positive bacteria, *Micrococcus luteus* (*M. luteus*, Gram-positive, ATCC 49732), to evaluate the bactericidal performance of CTO-NPs. Both types of bacteria (5.0 mL) were cultured in Difco™ nutrient LB broth (Miller Luria-Bertani, Becton-

Dickinson, Franklin Lakes, NJ) in an incubator shaker (Innova® 43, Incubator Shaker Series, New Brunswick Scientific, NJ) at 37 °C for 24 h.

The cultured bacteria (*S. marcescens* and *M. luteus*) were then diluted to 50 mL. The CTO-NPs (10, 100, and 1000 ppm) were tested against the above bacteria. After the treatment, an aliquot (0.5 mL) was collected and tested using ultraviolet visible spectroscopy (Lambda 35 ultraviolet-visible (UV-Vis) spectrophotometer (PerkinElmer, Fremont, CA)) to identify the absorbance every hour to determine the optical density (OD) at 600 nm (Fig. 1.17). Three doping amounts were tested in this study, indicating CTO-NPs are highly effective at inactivating bacteria under visible light. The observation indicated that Ce doping may result in the band gap of TiO_2 decrease (this assumption will be tested by synchronous X-ray).

The TEM images indicated high effectiveness using $Ce_{0.3}Ti_{0.7}O_2$ NPs on inactivation of both Gram-negative and Gram-positive bacteria, shown in Fig. 1.18. It can be seen that the cell membranes were peeling off and flagella disappeared, indicating the death of bacteria. Due to the active interaction between NPs and bacteria, it was assumed that the DNA fragmentation in cytosis was the mechanism to inactivate the bacteria. Although the Gram-positive bacteria (*M. luteus*) are generally considered more resilient to sterilization, this study showed similar trends observed for Gram-negative bacteria (*S. marcescens*). It was safe to conclude that minimal damage to the cell wall was observed, causing termination of cell division and damage of intact cell wall.

Elemental composition analyses by EDS (Fig. 1.19) also indicated cell death due to the permeability of calcium (Ca) and potassium (K) cations, and phosphorus (P) and nitrogen (N) anions across the cell membrane into the extracellular matrix for both microbes. "Ce" and "Ti" are from NPs used to inactivate bacteria; "P," "O," and "Cl" are from lipids on the membrane; "K" from the plasma membrane; and Cu is from the copper grid.

The CTO-NPs effectively inactivated Gram-negative microbes under visible light (TiO_2 requires UV). The kinetic study (Fig. 1.20) indicated that the $Ce_{0.35}Ti_{0.65}O_2$ photocatalyst follows the near-zero order reaction. The reaction orders for both $Ce_{0.20}Ti_{0.80}O_2$ and $Ce_{0.30}Ti_{0.70}O_2$ photocatalysts were found to be second order, approximately. However, the future work will be carried out to confirm the reaction order using CTO-NPs as disinfectants.

1.9 Discussion

1.9.1 Colloidal and Solid State Chemistry

Both colloidal and solid-state chemistry approaches were used to prepare Ce^{4+} ions doped TiO_2 nanoparticles (CTO-NPs). Different molar ratios between Ce and Ti were used to form 40 formulations of CTO-NPs. The temperatures to form CTO colloids were controlled at room temperature, while the calcination temperatures to produce CTO powders were controlled at 200–400 °C with an increment of 50 °C.

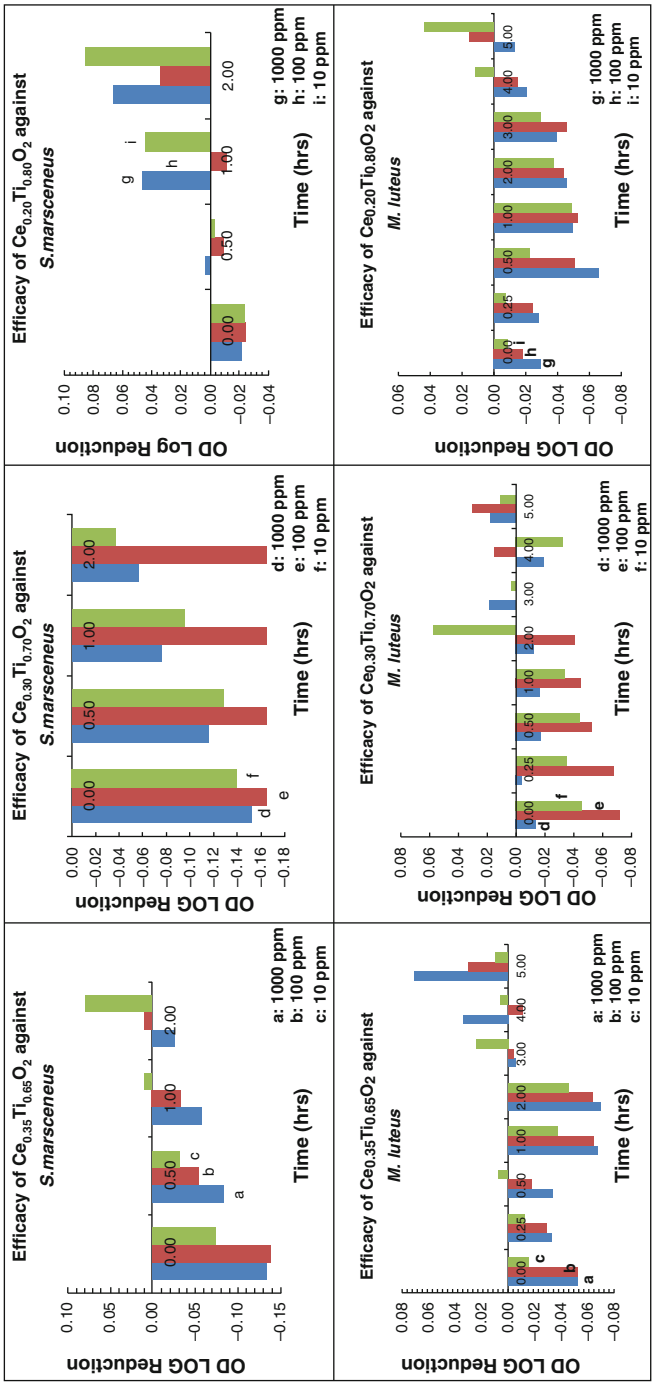

Fig. 1.17 (**a**) The bactericidal analyses of CTO-NPs: Gram-negative bacteria, *S. marcescens* cells were found to be damaged by CTO-NPs due to high particle-bacteria interaction. (**b**) The bactericidal analyses of CTO-NPs (three different Ce doping): Gram-positive bacteria, *M. luteus* cells were found to be damaged due to high particle-bacteria interaction

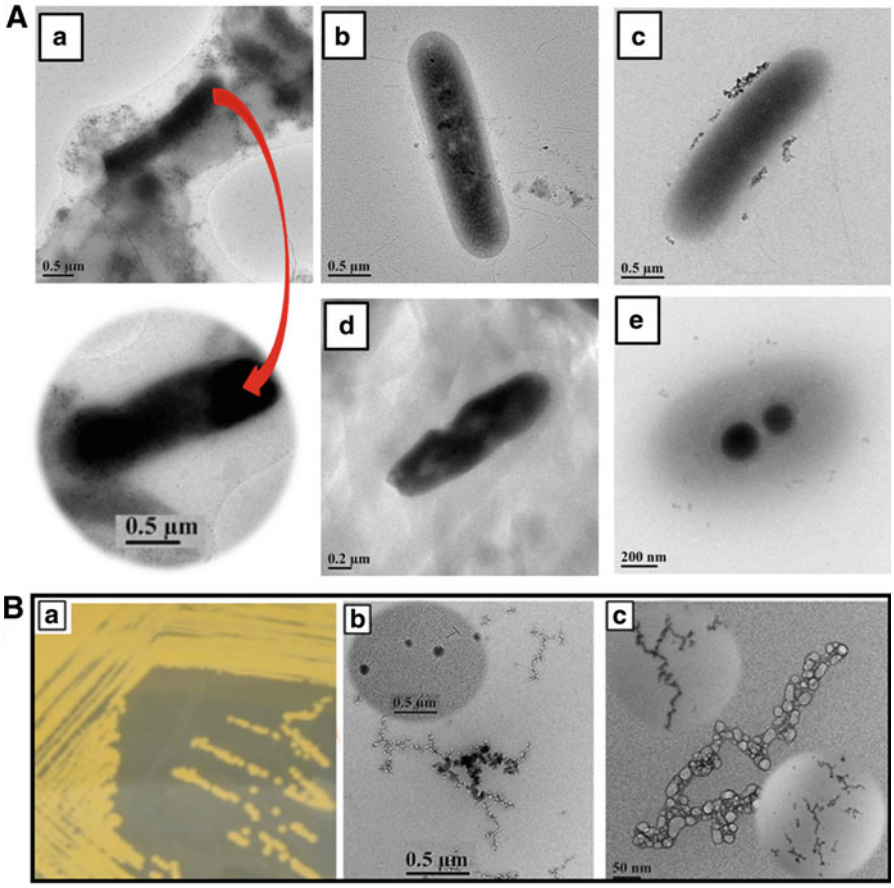

Fig. 1.18 (**a**) Transmission electron microscopy (TEM) image of a cluster of *S. marcescens* in varying stages of cell damage from *B* to *E*. The rod-shaped bacteria (*A*) were observed; *B* and *C*, the cell membrane was peeling out; and *D* and *E*, the flagella disappeared and DNA fragmented. (**b**) Optical Image of *M. luteus* adopted from *A* Ouverney and Zavala [118]; transmission electron microscopy (TEM) image of cluster of *M. luteus* in varying stages of cell damage from *B* to *C*. The potential residue of cells is observed; aggregation of microbial cell components and membrane sugars form the networks shaped structure

1.9.2 Characterization of Titania

Nano-characterization was employed to understand the in-depth structure of CTO-NPs. A series of the state-of-the-art techniques (five instrumental techniques) were used to characterize nanostructure. X-ray powder diffraction indicated highly crystalline anatase CTO-NPs were obtained, and crystallite sizes were tunable by varying the calcination temperatures. Spectroscopic and

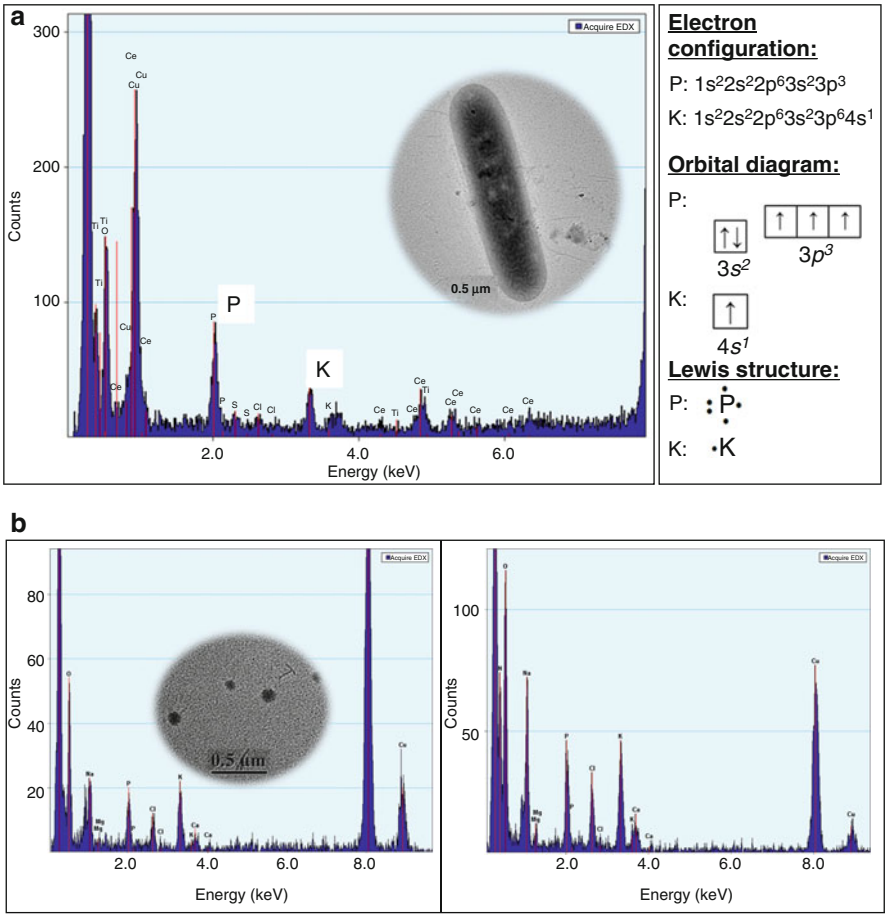

Fig. 1.19 (**a**) X-ray energy dispersive spectroscopy of elemental composition of *S. marcescens*. (**b**) X-ray energy dispersive spectroscopy of elemental composition of *M. luteus*

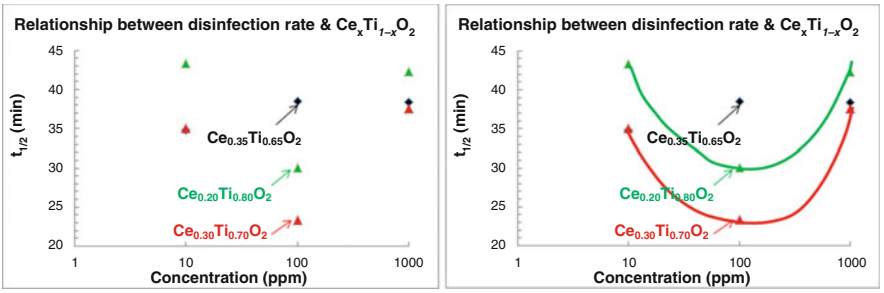

Fig. 1.20 Kinetic study by half-life to evaluate the bacteria inactivation reaction using CTO-NPs

microscopic analyses collectively provide instructive information to understand the fine structure of the CTO-NPs. To summarize, the characterization data provided a guideline to improve material design based on the end application.

1.9.3 Application of Nanomaterials

A recent study indicated that the dimensionality, particle size distribution, and crystallinity of TiO_2 nanoparticles are increasingly important to determine the electronic, optical, and biological properties and end applications of these nanoparticles. Traditionally, TiO_2-based nanomaterials have been extensively studied; however, photocatalytic and bactericidal activities under visible light have not been reported. The originality of this study lies in the application of CTO-NPs under visible light.

1.10 Conclusion

The following conclusions can be drawn from this study:

1. $Ce_xTi_{1-x}O_2$ NPs were fabricated using an ecologically friendly colloidal chemistry approach.
2. The nanoparticles were characterized as being monodispersive and crystalline (PDF 01-086-1157, 3.7852 × 9.5139 Å and 90 × 90°).
3. Although agglomeration of $Ce_xTi_{1-x}O_2$ NPs was detected, the photocatalytic reactivities and bactericidal performance were found be too effective.
4. Breaking down of methylene blue was observed under visible light without any UV light. The catalysts can be used in treating pharmaceutical wastes.
5. Inactivating both Gram-negative (*S. marcescens*) and Gram-positive (*M. luteus*) bacteria without introducing ultraviolet light. This study will provide a practical method for water disinfection.

Acknowledgments The authors wish to thank the National Science Foundation (CBET-0930079 and 0821370), Graduate Scholarship from the Department of Chemistry, Texas A&M University-Kingsville (TAMUK), the College of Arts and Sciences (CoA&S, Dr. Bashir, 160336-00002), ACS-PRF (53827-UR10, Liu), SFFP (Bashir) and Welch Departmental Grant (AC-0006, Dr. Hahn), NSF-MRI acquisition (Liu), URA (160315-00015, Liu) and RDF grants (160345-00005, Liu), at Texas A&M University-Kingsville (TAMUK) for funding.

Drs. E. Massa and J. Escudero (Department of Biological and Health Sciences, Texas A&M University-Kingsville, TAMUK) are acknowledged for providing bacteria. Dr. H. Kim and Ms. Y. Chen (Dr. H.-C. Zhou's group), Texas A&M University, College Station, are also duly acknowledged for image collection and analyses. The technical support from the TAMUK and the use of TAMU Center of Microscopy Imaging and Materials Characterization Facility are also duly acknowledged.

References

1. IAE Outlook, W.E., *International Energy Agency* (2017), pp. 1–782/782 pages, https://www.iea.org/weo2017/
2. M. Hasanuzzaman, U.S. Zubir, N.I. Ilham, H. Seng Che, Global electricity demand, generation, grid system, and renewable energy policies: a review. Wiley Interdisciplinary Rev. Energy Environ. **6**(3), e222 (2017)
3. EIA Outlook, A. E., Outlook with projections to 2050. January 5, 2017. *US Energy Information Administration* (2017), pp. 3–100/127 pages, https://www.eia.gov/outlooks/aeo/pdf/0383(2017).pdf
4. C. Philibert, *Solar Energy Perspectives*. (Organisation for Economic Co-operation and Development (OECD)/International Energy Agency (IEA)/IEA Publications/Imprimerie Centrale Printers, Luxembourg, 2011), pp. 1–228. 978-92-64-12457-8
5. Global, B. P., *BP Energy Outlook* 2017 (2017), pp. 1–103/103 pages, https://www.bp.com/content/dam/bp/pdf/energy-economics/energy-outlook-2017/bp-energy-outlook-2017.pdf
6. Burger, Willeke, Philipps et al., Research Projects. Fraunhofer Institute for Solar Energy Systems, ISE (2016), https://www.ise.fraunhofer.de/en/research-projects.html
7. GTMR, US Solar Market Insight, *GTM Research* (2017), https://www.greentechmedia.com/research
8. P. Mints, Insights & Experience. Next Generation Solar PV, Navigant Consulting (2017), https://www.navigantresearch.com/reports/next-generation-solar-pv
9. R. Pravalie, G. Bandoc, Nuclear energy: between global electricity demand, worldwide decarbonization imperativeness, and planetary environmental implications. J. Environ. Manag. **209**, 81–92 (2018)
10. C. Breyer, D. Bogdanov, A. Aghahosseini, A. Gulagi, M. Child, A.S. Oyewo, P. Vainikka, Solar photovoltaics demand for the global energy transition in the power sector, in *Progress in Photovoltaics: Research and Applications* (2017), pp. 505–523/693 pages
11. X. Lu, M.B. McElroy, J. Kiviluoma, Global potential for wind-generated electricity, in *Proceedings of the National Academy of Sciences*, 106(27), 10933–10938 (National Academy of Sciences, Washington DC, USA)
12. A. Méjean, C. Guivarch, J. Lefèvre, M. Hamdi-Cherif, The transition in energy demand sectors to limit global warming to 1.5 °C. Energy Effic., 12(2), 441–462, Springer Nature (Switzerland, AG) (2019)
13. M.J. Lynch, Peak oil, Chapter 2.17, in *Companion to Environmental Studies*. Routledge in association with GSE Research, Vol. 228, No. 231, ed. by N. Castree, M. Hulme, J. D. Proctor. (Taylor and Francis Group, Oxon, 2018), pp. 228–231/848. ISBN: 978-1-138-19220-1
14. M.Z. Jacobson, M.A. Delucchi, Z.A. Bauer, S.C. Goodman, W.E. Chapman, M.A. Cameron, J.R. Erwin, 100% clean and renewable wind, water, and sunlight all-sector energy roadmaps for 139 countries of the world. Joule **1**(1), 108–121 (2017)
15. C.J. Rhodes, Biofuel from algae: salvation from peak oil?, in *Seaweeds and Their Role in Globally Changing Environments* (Springer, Dordrecht, 2010), pp. 229–248/480 pages
16. A. Pérez-Tomás, E. Chikoidze, M. R. Jennings, S. A. Russell, F. H. Teherani, P. Bove, . . . & D. J. Rogers, Wide and ultra-wide bandgap oxides: where paradigm-shift photovoltaics meets transparent power electronics, in *Oxide-based Materials and Devices IX*, vol 10533, (International Society for Optics and Photonics, 2018), p. 105331Q
17. G. Gaither, U.S. Patent Application No. 10/017,053, 2018
18. B.P. Jelle, C. Breivik, H.D. Røkenes, Building integrated photovoltaic products: a state-of-the-art review and future research opportunities. Sol. Energy Mater. Sol. Cells **100**, 69–96 (2012)
19. ASTM, *G173-03 Standard Tables for Reference Solar Spectral Irradiances: Direct Normal and Hemispherical on 37° Tilted Surface* (ASTM International, West Conshohocken, 2012), pp. 1–3/20 pages, https://www.astm.org/Standards/G173.htm
20. B. Leckner, The spectral distribution of solar radiation at the earth's surface – elements of a model. Sol. Energy **20**(2), 143–150 (1978)

21. L.M. Perliski, S. Solomon, On the evaluation of air mass factors for atmospheric near-ultraviolet and visible absorption spectroscopy. J. Geophys. Res. Atmos. **98**(D6), 10363–10374 (1993)
22. L.C. Marquard, T. Wagner, U. Platt, Improved air mass factor concepts for scattered radiation differential optical absorption spectroscopy of atmospheric species. J. Geophys. Res. Atmos. **105**(D1), 1315–1327 (2000)
23. C.A. Gueymard, Parameterized transmittance model for direct beam and circumsolar spectral irradiance. Sol. Energy **71**(5), 325–346 (2001)
24. K.R. Lang, *Astrophysical data: Planets and stars*. (Springer, New York, 2012), pp. 3–78/937. 978-1-4684-0642-9
25. R. Russell, *The Multispectral Sun*. (Windows to the Universe.Org., 2017), https://www.windows2universe.org/sun/spectrum/multispectral_sun_overview.html
26. COMET, *Solar Radiation* (2018), http://www.comet.ucar.edu/
27. N. Li, M. Karin, Ionizing radiation and short wavelength UV activate NF-kB through two distinct mechanisms. Proc. Natl. Acad. Sci. **95**(22), 13012–13017 (1998)
28. N.S. Kapany, U.S. Patent No. 3,985,116. U.S. Patent and Trademark Office, Washington, DC, 1976
29. J. Zimmer, M. DiLabio, U.S. Patent Application No. 29/066,097, 1998
30. V.E. Cenusa, G. Darie, D. Tutica, M. Norisor, F.N. Alexe, C.M. Musat, Energetic and exergetic analysis of Rankine cycles for solar power plants with a parabolic trough and thermal storage. Renew. Energy Environ. Sustain. **1**, 10 (2016)
31. EIA, *Levelized Cost and Levelized Avoided Cost of New Generation Resources in the Annual Energy Outlook 2018* (US Energy Information Administration, 2018), pp. 1–20/20 pages, https://www.eia.gov/outlooks/aeo/pdf/electricity_generation.pdf
32. T. Tsoutsos, N. Frantzeskaki, V. Gekas, Environmental impacts of solar energy technologies. Energy Policy **33**(3), 289–296 (2005)
33. J. Peng, L. Lu, H. Yang, Review on life cycle assessment of energy payback and greenhouse gas emission of solar photovoltaic systems. Renew. Sust. Energ. Rev. **19**, 255–274 (2013)
34. D. Nugent, B.K. Sovacool, Assessing the lifecycle greenhouse gas emissions from solar PV and wind energy: a critical meta-survey. Energy Policy **65**, 229–244 (2014)
35. A. Goetzberger, C. Hebling, H.W. Schock, Photovoltaic materials, history, status, and outlook. Mater. Sci. Eng. R. Rep. **40**(1), 1–46 (2003)
36. H.W. Schock, Thin film photovoltaics. Appl. Surf. Sci. **92**, 606–616 (1996)
37. R.W. Miles, K.M. Hynes, I. Forbes, Photovoltaic solar cells: an overview of state-of-the-art cell development and environmental issues. Prog. Cryst. Growth Charact. Mater. **51**(1–3), 1–42 (2005)
38. M.E. Levinshtein, S.L. Rumyantsev, M.S. Shur (eds.), *Properties of Advanced Semiconductor Materials: GaN, AIN, InN, BN, SiC, SiGe* (Wiley, 2001), pp. 1–24, 31–44,49–65, 67–91, 93–143 and 146–186/216 pages
39. ElProCus, *Basic Structure of a Silicon Solar Cell* (ElProCus, 2018), https://elprocus.wordpress.com/2013/08/02/basic-structure-of-a-silicon-solar-cell/
40. M.A. Green, *Solar Cells: Operating Principles, Technology, and System Applications* (Prentice-Hall, Englewood Cliffs, 1982), pp. 1–9, 2–37, 4–59, 85–101 and 103–119/274 pages
41. L. El Chaar, N. El Zein, Review of photovoltaic technologies. Renew. Sust. Energ. Rev. **15**(5), 2165–2175 (2011)
42. C. Liu, J. Fan, H. Li, C. Zhang, Y. Mai, Highly efficient perovskite solar cells with substantial reduction of lead content. Sci. Rep. **6**, 35705 (2016)
43. M. Cardona, Y.Y. Peter, *Fundamentals of Semiconductors* (Springer, Berlin/Heidelberg, 2005), pp. 1–15, 17–105, 159–202 and 203–241/639 pages
44. A.G. Aberle, Thin-film solar cells. Thin Solid Films **517**(17), 4706–4710 (2009)
45. T.M. Razykov, C.S. Ferekides, D. Morel, E. Stefanakos, H.S. Ullal, H.M. Upadhyaya, Solar photovoltaic electricity: current status and future prospects. Sol. Energy **85**(8), 1580–1608 (2011)

46. N.G. Dhere, Present status and future prospects of CIGSS thin film solar cells. Sol. Energy Mater. Sol. Cells **90**(15), 2181–2190 (2006)
47. H. Spanggaard, F.C. Krebs, A brief history of the development of organic and polymeric photovoltaics. Sol. Energy Mater. Sol. Cells **83**(2–3), 125–146 (2004)
48. T.L. Benanti, D. Venkataraman, Organic solar cells: an overview focusing on active layer morphology. Photosynth. Res. **87**(1), 73–81 (2006)
49. V.V. Tyagi, N.A. Rahim, N.A. Rahim, A. Jeyraj, L. Selvaraj, Progress in solar PV technology: research and achievement. Renew. Sust. Energ. Rev. **20**, 443–461 (2013)
50. Q. Liu, Z. Liu, X. Zhang, N. Zhang, L. Yang, S. Yin, Y. Chen, Organic photovoltaic cells based on an acceptor of soluble graphene. Appl. Phys. Lett. **92**(22), 195 (2008)
51. B. O'regan, M. Grätzel, A low-cost, high-efficiency solar cell based on dye-sensitized colloidal TiO_2 films. Nature **353**(6346), 737 (1991)
52. U. Bach, D. Lupo, P. Comte, J.E. Moser, F. Weissörtel, J. Salbeck, M. Grätzel, Solid-state dye-sensitized mesoporous TiO_2 solar cells with high photon-to-electron conversion efficiencies. Nature **395**(6702), 583 (1998)
53. N.G. Park, Perovskite solar cells: an emerging photovoltaic technology. Mater. Today **18**(2), 65–72 (2015)
54. T. Horiuchi, H. Miura, K. Sumioka, S. Uchida, A high efficiency of dye-sensitized solar cells based on metal-free indoline dyes. J. Am. Chem. Soc. **126**(39), 12218–12219 (2004)
55. M.A. Green, K. Emery, Y. Hishikawa, W. Warta, E.D. Dunlop, Solar cell efficiency tables (version 47). Prog. Photovolt. Res. Appl. **24**(1), 3–11 (2015)
56. C.I. Ferreira, D.S. Kim, Techno-economic review of solar cooling technologies based on location-specific data. Int. J. Refrig. **39**, 23–37 (2014)
57. W. Shockley, H.J. Queisser, Detailed balance limit of efficiency of p-n junction solar cells. J. Appl. Phys. **32**(3), 510–519 (1961)
58. T. Tiedje, E. Yablonovitch, G.D. Cody, B.G. Brooks, Limiting efficiency of silicon solar cells. IEEE Trans. Electron Devices **31**(5), 711–716 (1984)
59. C. Downs, T.E. Vandervelde, Progress in infrared photodetectors since 2000. Sensors **13**(4), 5054–5098 (2013)
60. J.C. Shin, M. D'Souza, J. Kirch, L.J. Mawst, D. Botez, I. Vurgaftman, J.R. Meyer, Low temperature sensitive, deep-well 4.8 μm emitting quantum cascade semiconductor lasers, in *Lasers and Electro-Optics, 2009 and 2009 Conference on Quantum electronics and Laser Science Conference,* CLEO/QELS 2009. Conference on, IEEE, June 2009, pp. 1–2
61. A. Martí, A. Datas, J.R. González, C. Baur, Limiting efficiencies of novel solar cell concepts in space, in *E3S Web of Conferences,* vol. 16 (EDP Sciences, 2017), p. 03004
62. J. Wilson, Thermal issues in GaAs analog RF devices. Electron. Cooling **8**, 14–21 (2002)
63. M. Wagner, Simulation of thermoelectric devices. (Matr. Nr. *9925860)* Eingereicht An Der (*Technischen Universität Wien*) (Fakultät Für Elektrotechnik Und Informationstechnikvon, Bad Mitterndorf, 2007), http://www.iue.tuwien.ac.at/phd/mwagner/diss.html
64. Ioffe, *Silicon Electronic Properties* (*Ioffe,* 2018), http://www.ioffe.ru/SVA/NSM/Semicond/Si/electric.html
65. G.J. Snyder, E.S. Toberer, Complex thermoelectric materials, in *Materials for Sustainable Energy* (2011), V. Dusastre (Ed.), ISBN: 978-981-4317-66-5. World Scientific Publishing Co Pte Ltd (London, UK), pp. 101–110/360
66. Z.M. Gibbs, H.S. Kim, H. Wang, G.J. Snyder, Bandgap estimation from temperature dependent Seebeck measurement-deviations from the $2e|S|\max T_{max}$ relation. Appl. Phys. Lett. **106** (2), 022112 (2015)
67. Y.H. Kuo, Germanium-Silicon electroabsorption modulators, Doctoral dissertation, Stanford University, 2006, p. 20/107 pages, http://snowweb.stanford.edu/thesis/Kuo.pdf
68. Solar Cell Central, *Solar Efficiency Limits* (2018), http://solarcellcentral.com/limits_page.html
69. G.J. Snyder, T.S. Ursell, Thermoelectric efficiency and compatibility. Phys. Rev. Lett. **91**(14), 148301 (2003)
70. U.M. Gosele, Fast diffusion in semiconductors. Annu. Rev. Mater. Sci. **18**(1), 257–282 (1988)

71. PV Education, *Open-Circuit Voltage* (PV Education, 2018), https://www.pveducation.org/pvcdrom/open-circuit-voltage
72. V.K. Khanna, *Extreme-Temperature and Harsh-Environment Electronics*; Physics, technology and applications (2017), pp. 77–109/488. ISBN: 978-0-7503-1156-4. IOP Publishing, (Bristol, UK) IOP
73. P.N. Cheremisinoff, W.C. Dickinson (eds.), *Solar Energy Technology Handbook*, Part A (Marcel Dekker/Taylor and Francis Group, New York, 1980), pp. 483–499 and 500–515/882. ISBN: 0824768728
74. S. Kuravi, J. Trahan, D.Y. Goswami, M.M. Rahman, E.K. Stefanakos, Thermal energy storage technologies and systems for concentrating solar power plants. Prog. Energy Combust. Sci. **39** (4), 285–319 (2013)
75. J. Dostál, J. Pšencík, D. Zigmantas, In situ mapping of the energy flow through the entire photosynthetic apparatus. Nat. Chem. **8**(7), 705 (2016)
76. E. Singh, K.S. Kim, G.Y. Yeom, H.S. Nalwa, Atomically thin-layered molybdenum disulfide (MoS_2) for bulk-heterojunction solar cells. ACS Appl. Mater. Interfaces **9**(4), 3223–3245 (2017)
77. H. Kim, H.S. Kim, J. Ha, N.G. Park, S. Yoo, Empowering semi-transparent solar cells with thermal-mirror functionality. Adv. Energy Mater. **6**(14), 1502466 (2016)
78. A. Kojima, K. Teshima, Y. Shirai, T. Miyasaka, Organometal halide perovskites as visible-light sensitizers for photovoltaic cells. J. Am. Chem. Soc. **131**(17), 6050–6051 (2009)
79. X. Jiang, Z. Yu, Y. Zhang, J. Lai, J. Li, G.G. Gurzadyan, L. Sun, High-performance regular perovskite solar cells employing low-cost poly (ethylenedioxythiophene) as a hole-transporting material. Sci. Rep. **7**, 42564 (2017)
80. M. Chirumamilla, A.S. Roberts, F. Ding, D. Wang, P.K. Kristensen, S.I. Bozhevolnyi, K. Pedersen, Multilayer tungsten-alumina-based broadband light absorbers for high-temperature applications. Opt. Mater. Express **6**(8), 2704–2714 (2016)
81. M. Khalili, M. Abedi, H.S. Amoli, S.A. Mozaffari, Comparison of chitosan and chitosan nanoparticles on the performance and charge recombination of water-based gel electrolyte in dye-sensitized solar cells. Carbohydr. Polym. **175**, 1–6 (2017)
82. M. Freitag, J. Teuscher, Y. Saygili, X. Zhang, F. Giordano, P. Liska, A. Hagfeldt, Dye-sensitized solar cells for efficient power generation under ambient lighting. Nat. Photonics **11**(6), 372 (2017)
83. C. Winneker, *Global Market Outlook for Photovoltaics 2013–2017* (Construction21 International, 2013), http://www.construction21.org/articles/h/report–global-market-outlook-for-photovoltaics-2013-2017.html
84. X. Pan, I. Medina-Ramirez, R. Mernaugh, J. Liu, Nanocharacterization and bactericidal performance of silver modified titania photocatalyst. Colloids Surf. B: Biointerfaces **77**(1), 82–89 (2010)
85. Mindat, *Rutile Mineral Data* (Mindat, 2018), https://www.mindat.org/min-3486.html
86. W.S. Cho, B.C. Kang, J.K. Lee, J. Jeong, J.H. Che, S.H. Seok, Comparative absorption, distribution, and excretion of titanium dioxide and zinc oxide nanoparticles after repeated oral administration. Part. Fibre Toxicol. **10**(1), 9 (2013)
87. Mindat, *Anatase Mineral Data* (Mindat, 2018), https://www.mindat.org/min-213.html
88. Mindat, *Brookite Mineral Data* (Mindat, 2018), https://www.mindat.org/min-787.html
89. R. Kägi, A. Ulrich, B. Sinnet, R. Vonbank, A. Wichser, S. Zuleeg, M. Boller, Synthetic TiO_2 nanoparticle emission from exterior facades into the aquatic environment. Environ. Pollut. **156** (2), 233–239 (2008)
90. S. Dalai, S. Pakrashi, M.J. Nirmala, A. Chaudhri, N. Chandrasekaran, A.B.. Mandal, A. Mukherjee, Cytotoxicity of TiO_2 nanoparticles and their detoxification in a freshwater system. Aquat. Toxicol. **138**, 1–11 (2013)
91. S. Pakrashi, S. Dalai, T.C. Prathna, S. Trivedi, R. Myneni, A.M. Raichur, A. Mukherjee, Cytotoxicity of aluminum oxide nanoparticles towards freshwater algal isolates at low exposure concentrations. Aquat. Toxicol. **132**, 34–45 (2013)

92. B.J. Cardinale, R. Bier, C. Kwan, Effects of TiO_2 nanoparticles on the growth and metabolism of three species of freshwater algae. J. Nanopart. Res. **14**(8), 913 (2012)
93. J. Ji, Z. Long, D. Lin, Toxicity of oxide nanoparticles to the green algae *Chlorella* sp. Chem. Eng. J. **170**(2–3), 525–530 (2011)
94. V.P. Utgikar, N. Chaudhary, A. Koeniger, H.H. Tabak, J.R. Haines, R. Govind, Toxicity of metals and metal mixtures: analysis of concentration and time dependence for zinc and copper. Water Res. **38**(17), 3651–3658 (2004)
95. X. Zou, J. Shi, H. Zhang, Coexistence of silver and titanium dioxide nanoparticles: enhancing or reducing environmental risks? Aquat. Toxicol. **154**, 168–175 (2014)
96. V. Iswarya, M. Bhuvaneshwari, S.A. Alex, S. Iyer, G. Chaudhuri, P.T. Chandrasekaran, A. Mukherjee, Combined toxicity of two crystalline phases (anatase and rutile) of Titania nanoparticles towards freshwater microalgae: *Chlorella sp*. Aquat. Toxicol. **161**, 154–169 (2015)
97. A. Hassen, N. Saidi, M. Cherif, A. Boudabous, The resistance of environmental bacteria to heavy metals. Bioresour. Technol. **64**(1), 7–15 (1998)
98. S. Ramamoorthy, D.J. Kushner, Binding of mercuric and other heavy metal ions by microbial growth media. Microb. Ecol. **2**(2), 162–176 (1975)
99. A. Yamamoto, R. Honma, M. Sumita, Cytotoxicity evaluation of 43 metal salts using murine fibroblasts and osteoblastic cells. J. Biomed. Mater. Res. **39**(2), 331–340 (1998)
100. F. Heidenau, W. Mittelmeier, R. Detsch, M. Haenle, F. Stenzel, G. Ziegler, H. Gollwitzer, A novel antibacterial titania coating: metal ion toxicity and in vitro surface colonization. J. Mater. Sci. Mater. Med. **16**(10), 883–888 (2005)
101. A. Panas, C. Marquardt, O. Nalcaci, H. Bockhorn, W. Baumann, H.R. Paur, C. Weiss, Screening of different metal oxide nanoparticles reveals selective toxicity and inflammatory potential of silica nanoparticles in lung epithelial cells and macrophages. Nanotoxicology **7**(3), 259–273 (2012)
102. W. Lin, Y.W. Huang, X.D. Zhou, Y. Ma, In vitro toxicity of silica nanoparticles in human lung cancer cells. Toxicol. Appl. Pharmacol. **217**(3), 252–259 (2006)
103. J.L. Kang, C. Moon, H.S. Lee, H.W. Lee, E.M. Park, H.S. Kim, V. Castranova, Comparison of the biological activity between ultrafine and fine titanium dioxide particles in RAW 264.7 cells associated with oxidative stress. *J. Toxic. Environ. Health A* **71**(8), 478–485 (2008)
104. H.L. Karlsson, P. Cronholm, J. Gustafsson, L. Moller, Copper oxide nanoparticles are highly toxic: a comparison between metal oxide nanoparticles and carbon nanotubes. Chem. Res. Toxicol. **21**(9), 1726–1732 (2008)
105. C.M. Sayes, R. Wahi, P.A. Kurian, Y. Liu, J.L. West, K.D. Ausman, V.L. Colvin, Correlating nanoscale titania structure with toxicity: a cytotoxicity and inflammatory response study with human dermal fibroblasts and human lung epithelial cells. Toxicol. Sci. **92**(1), 174–185 (2006)
106. A. Simon-Deckers, B. Gouget, M. Mayne-L'Hermite, N. Herlin-Boime, C. Reynaud, M. Carriere, In vitro investigation of oxide nanoparticle and carbon nanotube toxicity and intracellular accumulation in A549 human pneumocytes. Toxicology **253**(1–3), 137–146 (2008)
107. S. Mayor, R.E. Pagano, Pathways of clathrin-independent endocytosis. Nat. Rev. Mol. Cell Biol. **8**(8), 603 (2007)
108. J. Kasper, M.I. Hermanns, C. Bantz, M. Maskos, R. Stauber, C. Pohl, J.C. Kirkpatrick, Inflammatory and cytotoxic responses of an alveolar-capillary coculture model to silica nanoparticles: comparison with conventional monocultures. Part. Fibre Toxicol. **8**(1), 6 (2011)
109. K.M. Waters, L.M. Masiello, R.C. Zangar, B.J. Tarasevich, N.J. Karin, R.D. Quesenberry, B.D. Thrall, Macrophage responses to silica nanoparticles are highly conserved across particle sizes. Toxicol. Sci. **107**(2), 553–569 (2008)
110. T. Morishige, Y. Yoshioka, H. Inakura, A. Tanabe, X. Yao, S. Narimatsu, Y. Mukai, The effect of surface modification of amorphous silica particles on NLRP3 inflammasome-mediated IL-1ß production, ROS production, and endosomal rupture. Biomaterials **31**(26), 6833–6842 (2010)

111. M. Winter, H.D. Beer, V. Hornung, U. Krämer, R.P. Schins, I. Förster, Activation of the inflammasome by amorphous silica and TiO_2 nanoparticles in murine dendritic cells. Nanotoxicology **5**(3), 326–340 (2011)
112. G.A. Orr, W.B. Chrisler, K.J. Cassens, R. Tan, B.J. Tarasevich, L.M. Markillie, B.D. Thrall, Cellular recognition and trafficking of amorphous silica nanoparticles by macrophage scavenger receptor A. Nanotoxicology **5**(3), 296–311 (2011)
113. H. Ruh, B. Kühl, G. Brenner-Weiss, C. Hopf, S. Diabaté, C. Weiss, Identification of serum proteins bound to industrial nanomaterials. Toxicol. Lett. **208**(1), 41–50 (2012)
114. C.M. Sayes, J.D. Fortner, W. Guo, D. Lyon, A.M. Boyd, K.D. Ausman, J.L. West, The differential cytotoxicity of water-soluble fullerenes. Nano Lett. **4**(10), 1881–1887 (2004)
115. A. Selloni, A. Vittadini, M. Grätzel, The adsorption of small molecules on the TiO_2 anatase (101) surface by first-principles molecular dynamics. Surf. Sci. **402**, 219–222 (1998)
116. A. Vittadini, A. Selloni, F.P. Rotzinger, M. Grätzel, Structure and energetics of water adsorbed at TiO_2 anatase\(101\) and\(001\) surfaces. Phys. Rev. Lett. **81**(14), 2954 (1998)
117. C.M. Sayes, A.M. Gobin, K.D. Ausman, J. Mendez, J.L. West, V.L. Colvin, Nano-C60 cytotoxicity is due to lipid peroxidation. Biomaterials **26**(36), 7587–7759 (2005)
118. C. Ouverney, V.E. Zavala, *Microbiology Laboratory # 9. Images of Common Microorganism, Grown on Nutrient Agar*. (San Jose State University, San Jose, 2018).